ORCA – Online Research @ Cardiff

A Non-Singular Boundary Element Method for Modelling Bubble Dynamics in Viscoelastic Fluids

M. Walters, T.N. Phillips[1]

School of Mathematics, Cardiff University, Senghennydd Road, Cardiff CF24 4AG, United Kingdom

---

Abstract

When a cavity forms near a solid boundary a liquid jet can form directed towards the boundary, causing the generation of high pressures at the wall (potentially causing damage) and the formation of a toroidal bubble. In this paper several recent developments in the boundary element modelling of the dynamics of cavitation bubbles in viscoelastic fluids are presented. The standard formulation of the boundary element method (BEM) is in terms of a boundary integral equation with a singular kernel. A reformulation of the BEM in terms of a non-singular kernel is shown to provide enhanced stability. In situations when a liquid jet forms and impacts the far side of the bubble there is a transition to a toroidal form. This topological singularity in bubble geometry is modelled by placing a vortex ring inside the bubble to account for the circulation in the fluid and the discontinuity in potential following jet impact. The bubble dynamics are dependent on the initial stand-off distance from the boundary as well as the viscous and elastic properties of the fluid. It is shown that, while the viscosity of the fluid inhibits jet formation, the dynamics are particularly dependent on the relative strength of viscous, elastic and inertial forces. In particular, if the Deborah number is large enough elastic effects effectively negate fluid viscosity and behaviour similar to the inviscid case is recovered in terms of liquid jet formation.

Keywords: Non-singular, boundary element, cavitation, bubble, vortex ring, viscoelasticity

---

[1]Corresponding author, Email:PhillipsTN@cf.ac.uk, Phone: +44 2920 874194, FAX: +44 2920 874199

1. Introduction

Despite their small size, cavitation bubbles can exhibit extreme physics with immense increases in pressure and temperature occurring during collapse. Their tendency to focus and concentrate energy, forces and stresses as well as emitting shockwaves means that they have the potential to cause damage to nearby surfaces and structures. This destructive behaviour has been utilised to advantage in a number of biomedical applications such as extracorporeal shock wave lithotripsy (ESWL) [35], ultrasound contrast imaging [9] and sonoporation [29]. An understanding of the behaviour of cavitation bubbles is essential to improve the effectiveness of each of these distinct procedures and to ensure that damage is restricted to the targeted areas.

The dynamics of an initially spherical bubble in an infinite extent of fluid was originally studied by Lord Rayleigh [37], motivated by the damage caused to ship's propellers from collapsing cavitation bubbles. The dynamics is described by the Rayleigh Plesset equation, the solution of which provides the evolution of the bubble radius.

Early theoretical work modelling a bubble near a rigid wall [36, 46] was based on perturbations of the spherically symmetric solution developed by Rayleigh [37]. Later, Chahine and Bovis [12] extended this perturbation analysis to include the effects of surface tension using matched asymptotic expansions in powers of a small parameter ϵ defined by

$$\epsilon = \frac{R_m}{h}, \tag{1}$$

where R_m and h are the maximum bubble radius and distance from the centre of the bubble to the wall, respectively. However, this analysis is only valid for small values of ϵ and therefore is not applicable for the cases of interest in this paper where the bubble is near the wall for which $\epsilon \approx 1$. An alternative theoretical study was undertaken by Naude [31] who solved the Laplace equation for the velocity potential using Legendre polynomials and extended the theory to allow for larger perturbations.

The development of high-speed cameras allowed accurate photographs of bubble shape to be captured, the most notable early experimental study was that of Benjamin and Ellis [2]. Their experiments involved a Perspex sheet with cavities grown from nuclei situated at various small distances from it. The main phenomena captured in their experiments were the formation of a liquid jet in the direction of the rigid wall and the subsequent transition

to a toroidal form. Benjamin and Ellis also seem to have been the first to realise the importance of the Kelvin Impulse in cavitation bubble dynamics. The Kelvin Impulse is the apparent inertia of the cavitation bubble and can be used to determine the direction of the bubble centroid and liquid jet [4]. Lauterborn and Bolle [23] measured jet velocities up to 120m/s for a bubble near a solid plate and observed a small counterjet away from the boundary due to the bubble being driven towards the wall during collapse.

Early developments in numerical methods for bubble dynamics included the marker and cell method [30] which enabled the later stages of collapse to be predicted, beyond what was possible using perturbation techniques. The first fully numerical paper for describing the complete collapse of a cavitation bubble near a rigid wall was by Plesset and Chapman [34]. They developed a finite difference method based on cylindrical coordinates with the velocity potential determined from boundary conditions at the surfaces and at infinity. Their model demonstrated a remarkable agreement with the experiments of Lauterborn and Bolle [23] and, in particular, predicted the formation of a liquid jet.

To model a non-spherical bubble, the boundary element method (BEM) is often used. The BEM requires significantly less computational time and memory compared to other numerical methods such as finite elements or spectral elements since only the boundary is discretised. An additional advantage of BEM is that it is able to model the bubble surface as a true discontinuity obviating the need to employ sophisticated interface tracking techniques. The BEM was originally used to model a cavitation bubble by Guerri et al. [14]. It was further developed by Blake et al. [5, 6] who considered the dynamics of an axisymmetric, vapour-filled bubble near a rigid wall and free surface. Since these early works a plethora of extensions of BEM have followed which have included the effects of buoyancy [43], elasticity [19] and viscoelasticity [27, 42]. In terms of bubble topology extensions have included treatment of curved surfaces [41] and toroidal bubbles [3, 47, 44].

Improvements have also been made to BEM in terms of the accuracy of the discretisation of the bubble surface through the use of high-order (cubic and quintic) splines [25, 42]. The improved accuracy of these spline discretisations mean that far fewer nodes are required to discretise the bubble surface, leading to improved computational performance. The standard BEM formulation in terms of a boundary integral equation contains kernels that are singular due to the divergence of the Green's function and its derivative around the source point. Additionally, when two nodes on the surface are

3

close, near-singular behaviour leads to ill-conditioned linear systems. In this paper, a non-singular BEM formulation based on ideas of Klaseboer et al. [39] is developed for predicting bubble dynamics in the vicinity of a rigid wall. The non-singular formulation removes these singularities at the outset leading to a formulation of the BEM that is much more numerically stable.

The non-singular BEM formulation is found to dramatically reduce numerical errors produced by nodes becoming too close together. Consequently, the smoothing schemes typically used in the standard BEM formulation are no longer required to produce smooth bubble profiles. The use of quintic splines is shown to be more efficient than cubic splines in terms of the number of nodes required to attain a prescribed accuracy. The dynamics of a bubble in an Oldroyd-B fluid are found to be determined by a competition between viscous, elastic and inertial forces. Typically, viscous effects tend to reduce velocities and to inhibit jet formation although this can be negated by the elasticity of the fluid. For certain values of Reynolds and Deborah numbers a strong liquid jet occurs in the direction of the boundary, similar to the inviscid case. In contrast, however, the bubble centre is much thinner, resulting in the bubble rebounding away from the wall and negative pressures being generated.

2. Mathematical Model

Consider a bubble initially spherical in shape and whose centroid is a distance h, known as the initial stand-off distance, from a rigid boundary of infinite extent. It is assumed that the bubble remains axisymmetric for all time, effectively reducing the dimension of the problem. Inherent in this assumption is that the bubble is stable to distortions from symmetry. Although this is not always the case, it is generally found to be true for small cavitation bubbles [7]. Additionally, the axisymmetric case can be seen as providing the instance of maximum jet speeds and pressures and thus is an indicator of maximum potential damage to nearby surfaces. It is also assumed that the fluid is incompressible and irrotational.

Since we are concerned with high speed bubble growth/collapse phenomena, it is reasonable to assume that the flow is inertia dominated in the bulk with viscous and viscoelastic effects being negligible. However, there are always thin boundary layers near the bubble where these effects can be appreciable due to the need to satisfy the physical stress boundary conditions. The thickness of the boundary layer depends on the competing influences of

viscosity and elasticity and is approximately $1/\sqrt{(ReDe)}$. This justifies neglecting viscous diffusion when elastic effects are dominant and demonstrates that even for moderate Re there is a return to inviscid behaviour in this case. Hence, the assumption that the entirety of the flow is irrotational with viscous and viscoelastic effects appearing through the normal stress balance at the bubble/free surface provides a consistent description of the physical problem. Despite not offering a solution to the full equations of motion, the irrotational assumption, at the very least, provides important and relevant insights into the dynamics of the problem.

In order to formulate a velocity potential, ϕ, which satisfies the Laplace equation, it is necessary to assume incompressibility. The primary condition needed for this approximation to be valid is [1]

$$M^2 \ll 1, \tag{2}$$

where $M = \frac{U}{c}$ is the Mach number, c is the speed of sound in the liquid and U is the magnitude of variations of the fluid velocity with respect to both position and time. It is reasonable to assume incompressibility if $M^2 < 0.2$. Brujan [8] noted that in the late stages of collapse when a jet forms the bubble wall velocities can approach the speed of sound which means that the condition (2) is violated and liquid compressibility can no longer be ignored. These high velocities also give rise to very large pressures in the fluid.

Although methods based on potential theory predict initial bubble dynamics very well they can break down in the final stages of collapse when compressibility effects become important due to their inability to simulate shock waves, for example. Recent work has focused on developing methods capable of solving the Euler equations in order to handle shock waves and interfaces in a robust fashion. For example, So et al. [38] have developed an interface sharpening method for two-phase compressible flow simulations based on solving an anti-diffusion equation for the volume-fraction field that counteracts the numerical diffusion resulting from the underlying VOF discretization scheme. Johnsen and Colonius [16] have developed a high-order accurate shock- and interface-capturing scheme using a weighted essentially non-oscillatory (WENO) scheme to simulate the collapse of a gas bubble in water. However, an accurate treatment of compressible effects has yet to be incorporated into viscoelastic cavitation modelling.

Note that possible limitations of the incompressible model presented in this paper are that neither the shock wave generated at jet impact nor the

5

wave reflected back into the bubble is modelled. Note that in real-life situations, a shock wave would be generated if the bubble initially expands at a speed larger than the speed of sound of the surrounding liquid medium. This may happen for cases for which the normalized initial bubble pressure is large. The initial shock travels well ahead of the bubble surface. While the amplitude of the pressure pulse generated by the shock wave on the wall is usually much larger than that due to liquid jet impingement, its duration is much shorter and associated impulse smaller. This is a reason why we have chosen to employ the simpler incompressible flow model, as others have also done [11, 44, 21]. Since the incompressible flow model is not able to account for the effects due to the initial shock wave, this should be borne in mind when interpreting the pressure results in all incompressible flow computations.

Brujan et al. [11] studied the final stage of the collapse of a laser-produced cavitation bubble close to a rigid boundary both experimentally and theoretically. In particular, the temporal evolution of the liquid jet developed during bubble collapse, shock wave emission and the behaviour of the 'splash' effect were investigated using high-speed photography with up to 5 million frames/second. Numerical simulations were conducted using a boundary integral method with an incompressible liquid impact model. The experimental and numerical data compared very favourably in terms of both the bubble shape history and the translational motion of the bubble. Klaseboer et al. [21] modelled the interaction of a step pressure wave with a bubble ignoring the wave transmitted through the bubble and any reflection off the bubble surface. However, predictions using this model agreed remarkably well with FLM and ALE (compressible) simulations which include shock scattering. Although some differences are observed in the early and late stages, as one would expect, the overall conclusion suggests the behaviour is still inertia dominated and internal shock waves in the bubble are of secondary importance.

Lind and Phillips [27, 28] provide evidence that demonstrates that the BEM is able to reproduce phenomena observed in experiments. For the collapse of cavitation bubbles near a rigid boundary, Lind and Phillips [27] showed that numerical predictions for the maximum jet velocity compared very favourably with the experimental measurements of Brujan et al. [10]. In the experimental study, the dynamics of ultrasound induced bubbles were investigated in three different fluids: water, a 0.5% polyacrylamide (PAM) aqueous solution, and a 0.5% carboxymethylcellulose (CMC) aqueous solution. It was found that the maximum jet velocity diminished with the

6

addition of polymer additives, with the most significant reduction found in the more elastic PAM solution. The experimentally determined values given for the zero-shear viscosity are used in the simulations, while the relaxation times used are of a similar order to those suggested in [10]. The general trend observed in the experiment is reproduced viz. jet velocity reduction is most significant in the PAM solution, than in the CMC solution. Additionally, the maximum jet velocities obtained for each fluid are also similar in magnitude to those obtained experimentally. Additionally, Lind and Phillips [28] investigated nonspherical bubble collapse near a free surface. Experimental results by Chahine [13] on bubble collapse in water and polymeric solutions were used to make comparisons with numerical predictions. Comparisons between experimental measurements and numerical predictions were presented for both water and the polymeric solution water/polyox for different initial stand-off distances of the bubble from the free surface. Close agreement was obtained between the experiments and the numerical simulations that highlight the initial elongation of the bubble along the axis and the subsequent bubble collapse. These comparisons confirm that the mathematical model for bubble dynamics described in this paper can be used to predict phenomena observed for real fluids.

It is assumed that the bulk viscosity of the fluid is negligible. The effects of viscosity and fluid rheology are typically only important in thin boundary layers near the bubble surface and thus can be approximately modelled through a boundary condition at the bubble interface [1, 26]. This approximation has been justified and used in Lind and Phillips [26] and Walters [42]. Comparisons of predictions using BEM with the direct solution of the Rayleigh-Plesset equation for a spherical bubble have shown that qualitatively similar results are produced but with the BEM model predicting slightly larger amplitude oscillations [42].

2.1. Governing Equations

Since the fluid is assumed to be incompressible the dynamic laws for the fluid are given by

$$\nabla \cdot \mathbf{u} = 0, \tag{3}$$

$$\rho \frac{\mathrm{D}\mathbf{u}}{\mathrm{D}t} = -\nabla p + \nabla \cdot \boldsymbol{\tau}, \tag{4}$$

where D/Dt is the material derivative, ρ is the density, $\mathbf{u}$ is the fluid velocity field, p is the pressure and $\boldsymbol{\tau}$ is the deviatoric stress tensor.

The assumption of irrotationality implies the existence of a velocity potential ϕ with $\mathbf{u} = \nabla\phi$, which satisfies Laplace's equation in the fluid domain

$$\nabla^2\phi = 0. \tag{5}$$

Thus, in general, one cannot simultaneously prescribe normal and tangential velocities at a rigid wall for irrotational flows of incompressible fluids. Since the rigid wall is a bounding surface it must always be in contact with the fluid so it is the no-penetration condition that must be prescribed. Joseph et al. [17] provide many examples of irrotational flows of viscous fluids which approximate exact solutions of the Navier-Stokes equations and agree with experiments at low Reynolds numbers.

In terms of ϕ, the momentum equation (4) can be written in the form

$$\nabla\left(\rho\frac{\partial\phi}{\partial t} + \frac{\rho}{2}|\nabla\phi|^2 + p\right) = \nabla\cdot\boldsymbol{\tau}. \tag{6}$$

Equation (6) can be integrated to give an irrotational equation of motion provided that the compatibility condition

$$\nabla\cdot\boldsymbol{\tau} = \nabla\varphi, \tag{7}$$

is satisfied for some scalar function φ.

Joseph and co-workers (see [18], for example) considered the compatibility of general constitutive equations with general irrotational flows. Although it can be shown that Bernoulli equations are indeed admissible for inviscid and viscous Newtonian fluids and for the linear Maxwell fluid (with $\varphi = 0$ in each case), the majority of established viscoelastic models are generally inadmissible i.e. $\nabla\times\nabla\cdot\boldsymbol{\tau} \neq 0$ for general $\boldsymbol{\tau}$, even though $\nabla\times\mathbf{u} = 0$. There is an incompatibility in the theory of viscoelastic potential flow. Although some simple linear viscoelastic models are admissible, they are not frame invariant. Furthermore, they can only provide meaningful predictions in the limit of small fluid deformations. However, under the assumptions described above, the admissibility condition can be satisfied in an approximate sense for moderate to large Reynolds numbers since $\nabla\cdot\boldsymbol{\tau}$ becomes small compared to inertial terms in the momentum equation in the bulk of the flow. Thus more general models, such as the material Maxwell model, can be employed that provide a more accurate description of viscoelastic effects and also satisfy frame invariance. Note that the restriction to moderate and high Reynolds number flows limits the method to modelling dilute polymer solutions.

8

Therefore, since viscoelastic effects are introduced only through the boundary conditions, it has been assumed that the bulk viscosity is negligible and thus (7) holds. Then integrating equation (6) gives

$$\rho\frac{\partial\phi}{\partial t} + \frac{\rho}{2}|\nabla\phi|^2 + p - \varphi = C(t),\tag{8}$$

for some function $C(t)$. Noting that ϕ, $\varphi \to 0$ as $t \to \infty$ gives $C(t) = p_\infty$, the (undisturbed) pressure at infinity. Then, evaluating (8) at the bubble surface yields

$$p_B = -\rho\frac{\mathrm{D}\phi}{\mathrm{D}t} + \frac{\rho}{2}|\nabla\phi|^2 + p_\infty\tag{9}$$

where p_B is the pressure on the liquid side of the bubble surface, φ has been taken to be zero and $\mathrm{D}/\mathrm{D}t$ is the material derivative. Assuming there is no mass transfer through the bubble surface, the balance of normal forces across the surface gives

$$\sigma_{nn}(\text{liquid}) = -p_B + \tau_{nn} = \sigma_{nn}(\text{gas}) + \sigma\kappa = -p_i + \sigma\kappa\tag{10}$$

where σ is the (static) surface tension, κ is the curvature and p_i is the internal bubble pressure. Note that equation (10) also assumes the bubble interface is 'clean' (no surfactants present) and only the normal component is required since the bubble interface is a stress-free free surface. Finally, combining (9) and (10) to eliminate p_B gives the Bernoulli equation, used to update the velocity potential ϕ

$$\rho\frac{\mathrm{D}\phi}{\mathrm{D}t} = \frac{\rho}{2}|\nabla\phi|^2 - \tau_{nn} + \sigma\kappa + p_\infty - p_i.\tag{11}$$

Since the bubble surface is stress-free, fluid particles which begin on the surface will remain there and thus the surface can be updated in a Lagrangian manner

$$\frac{\mathrm{D}\mathbf{x}}{\mathrm{D}t} = \nabla\phi,\tag{12}$$

where $\mathbf{x}$ is a point on the surface. The internal bubble pressure is modelled using

$$p_i(t) = p_0\left(\frac{R_0}{R}\right)^{3\lambda},\tag{13}$$

where λ is the ratio of specific heats for the gas and p_0 is the (initial) internal pressure.

2.2. Calculation of the Extra Stress Tensor

For a Newtonian fluid the extra stress tensor is given by

$$\boldsymbol{\tau} = \mu\left((\nabla \mathbf{u}) + (\nabla \mathbf{u})^T \right) = 2\mu(\nabla \mathbf{u}), \tag{14}$$

since the assumption of irrotationality implies the velocity gradient is symmetric [1]. The required normal component τ_{nn} is then given by

$$\tau_{nn} = 2\eta_s \frac{\partial^2 \phi}{\partial n^2}. \tag{15}$$

To model fluid rheology the Oldroyd-B model is chosen since it is sophisticated enough to model a range of rheological behaviour while still being relatively simple to implement. For the Oldroyd-B model the polymeric stress $\boldsymbol{\tau}$ can be expressed [33] in terms of its solvent and polymeric contributions

$$\boldsymbol{\tau} = \boldsymbol{\tau}^s + \boldsymbol{\tau}^p, \tag{16}$$

where

$$\boldsymbol{\tau}^s = 2\eta_s \nabla \mathbf{u}, \quad \boldsymbol{\tau}^p + \lambda_1 \overset{\triangledown}{\boldsymbol{\tau}^p} = 2\eta_p \nabla \mathbf{u}, \tag{17}$$

and $\overset{\triangledown}{\boldsymbol{\tau}}$ denotes the upper-convected derivative of $\boldsymbol{\tau}$ defined by

$$\overset{\triangledown}{\boldsymbol{\tau}} = \frac{\partial \boldsymbol{\tau}}{\partial t} + \mathbf{u} \cdot \nabla \boldsymbol{\tau} - (\nabla \mathbf{u})^T \cdot \boldsymbol{\tau} - \boldsymbol{\tau} \cdot (\nabla \mathbf{u}). \tag{18}$$

In these equations η_s, η_p and λ_1 are the solvent viscosity, polymeric viscosity and relaxation time of the fluid, respectively.

2.3. Updating the System in Time

The following equations have been derived to update the bubble surface as well as the velocity potential and normal stress thereon

$$\frac{D\mathbf{x}}{Dt} = \nabla \phi, \tag{19}$$

$$\rho \frac{D\phi}{Dt} = \frac{\rho}{2}|\nabla \phi|^2 - 2\eta_s \frac{\partial^2 \phi}{\partial n^2} - \tau_{nn}^p + \sigma \kappa + p_\infty - p_0 \left(\frac{V_0}{V} \right)^\lambda, \tag{20}$$

$$\lambda_1 \frac{D\tau_{nn}^p}{Dt} = -\tau_{nn}^p - 2\lambda_1 \tau_{nn}^p \frac{\partial^2 \phi}{\partial n^2} - 2\eta_p \frac{\partial^2 \phi}{\partial n^2}. \tag{21}$$

For a Newtonian fluid, $\tau_{nn}^p = 0$ obviating the need to solve (21).

10

2.3.1. Non-Dimensionalisation

The variables are non-dimensionalised using

$$r^* = \frac{r}{R_m}, \quad z^* = \frac{z}{R_m}, \quad t^* = \frac{U}{R_m}t, \quad \phi^* = \frac{\phi}{UR_m} \tag{22}$$

where R_m is the maximum bubble radius attained by a single gas bubble in an inviscid infinite fluid and $U = (P_{ref}/\rho)^{1/2}$ is used as a characteristic velocity. The pressure term $p_\infty = P_{ref} = 1 \times 10^5 \mathrm{Pa}$ is atmospheric pressure. Using this non-dimensionalisation the Deborah, Reynolds and Weber numbers are

$$De = \frac{\lambda_1}{R_m}\left(\frac{P_{ref}}{\rho}\right)^{1/2}, \quad Re = \frac{R_m((P_{ref})\rho)^{1/2}}{\eta}, \quad We = \frac{\rho U^2 R_m}{\sigma} = \frac{R_m P_{ref}}{\sigma}. \tag{23}$$

To update the system in time the system of equations (19)-(21) is integrated using a fourth-order Runge-Kutta time stepping scheme. The dimensionless time step is chosen to be

$$\triangle t = \frac{\triangle t_{\max}}{\max(\mathrm{D}\phi^*/\mathrm{D}t^*)}, \tag{24}$$

where $\triangle t_{\max}$ is the maximum dimensionless time step chosen to be 10^{-3}, unless otherwise stated. The time step has been chosen to deal with the rapidly changing velocity that can occur during bubble collapse; for large velocities the time step is reduced in order to capture the high speed dynamics of the bubble.

3. Standard Boundary Element Method

Green's third integral identity can be used to show that ϕ satisfies the boundary integral equation

$$c(\mathbf{p})\phi(\mathbf{p}) = \int_{\partial\Omega}\left(\frac{\partial\phi}{\partial n}(\mathbf{q})G(\mathbf{p},\mathbf{q}) - \phi(\mathbf{q})\frac{\partial G}{\partial n}(\mathbf{p},\mathbf{q})\right)dS, \tag{25}$$

where $c(\mathbf{p})$

$$c(\mathbf{p}) = \begin{cases} 2\pi & \text{if } \mathbf{p} \in \partial\Omega \\ 4\pi & \text{if } \mathbf{p} \in \Omega\backslash\partial\Omega, \end{cases}$$

11

and Ω, $\partial\Omega$ are the fluid domain and its boundary, respectively. Here $\mathbf{p}$ and $\mathbf{q}$ are points in the fluid and on the boundary, respectively, which can be expressed in Cartesian coordinates as

$$\mathbf{p} = (r_0, 0, z_0), \quad \mathbf{q} = (r\cos\theta, r\sin\theta, z). \tag{26}$$

Note that the second component of $\mathbf{p}$ can be taken to be zero without loss of generality, due to the axisymmetric nature of the problem. In an infinite fluid, the 3D Green's function is

$$G_1(\mathbf{p}, \mathbf{q}) = \frac{1}{|\,\mathbf{p} - \mathbf{q}\,|}. \tag{27}$$

In the case of a bubble situated near a rigid wall the domain of integration $\partial\Omega$ includes the wall. In order to simplify the integral to one defined over the bubble surface only a modified Green's function is used

$$G(\mathbf{p}, \mathbf{q}) = G_1(\mathbf{p}, \mathbf{q}) + G_1(\mathbf{p}', \mathbf{q}) \tag{28}$$

where $\mathbf{p}' = (r_0, 0, -z_0)$ is the image point of $\mathbf{p}$ (reflected in the rigid wall). The modified Green's function results in ϕ satisfying the no penetration condition

$$\frac{\partial\phi}{\partial z} = 0 \quad \text{at} \quad z = 0, \tag{29}$$

and alleviates the need to integrate over the rigid wall. Substituting the Cartesian forms of $\mathbf{p}$ and $\mathbf{q}$ into (27) yields

$$G_1(\mathbf{p}, \mathbf{q}) = \frac{1}{[(r + r_0)^2 + (z - z_0)^2 - 4rr_0\cos^2(\frac{\theta}{2})]^{1/2}}, \tag{30}$$

with normal derivative

$$\frac{\partial G_1}{\partial n} = \frac{-(r - r_0\cos\theta)n_r - (z - z_0)n_z}{[(r + r_0)^2 + (z - z_0)^2 - 4rr_0\cos^2(\frac{\theta}{2})]^{3/2}}, \tag{31}$$

where the normal vector is $\mathbf{n} = (n_r, 0, n_z)$.

3.1. Discretisation

The bubble surface is decomposed into N segments, as shown in Fig. 1. In the standard BEM, equation (25) is discretised to give

$$c(\mathbf{p}_i)\phi(\mathbf{p}_i) + \sum_{j=1}^{N}\int_{s_j}^{s_{j+1}}\phi(\mathbf{q})\frac{\partial G}{\partial n}(\mathbf{p}_i, \mathbf{q})dS = \sum_{j=1}^{N}\int_{s_j}^{s_{j+1}}\frac{\partial\phi_i}{\partial n}(\mathbf{q})G(\mathbf{p}_i, \mathbf{q})dS. \tag{32}$$

for each node $i = 1, \ldots, N + 1$, where s_j is the arclength at node j. If the segment being integrated over contains the collocation point $\mathbf{p}_i$ then a weak logarithmic singularity occurs. This is typically treated by splitting the integral into non-singular and singular contributions and approximating the latter using a log-Gaussian quadrature rule.
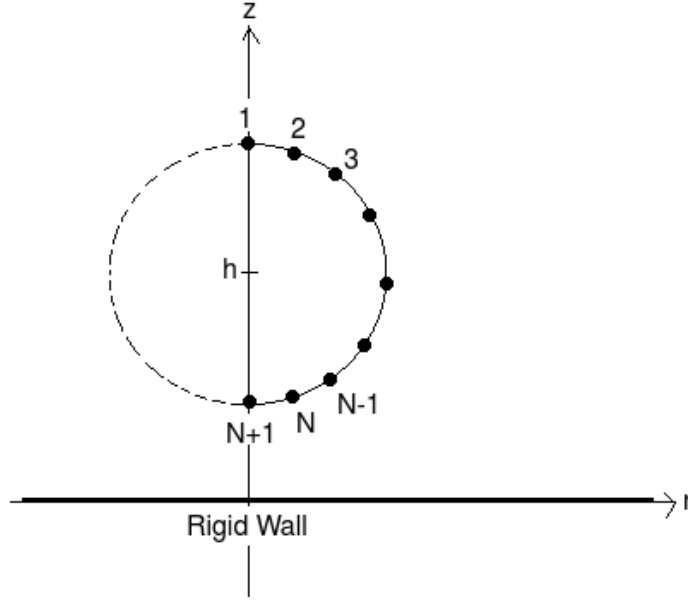
Figure 1: Discretisation of the bubble surface into N segments.

4. Non-singular BEM Formulation

Following Klaseboer et al. [39], in order to remove the singularities from the boundary integral equation functions ψ_i, $i = 1, \ldots, N + 1$, defined by

$$\psi_i(\mathbf{p}) = \phi(\mathbf{p}_i) + \left(\frac{\partial \phi}{\partial n} \right)_i f_i(\mathbf{p}), \tag{33}$$

are constructed where the functions f_i satisfy

$$\nabla^2 f_i(\mathbf{p}) = 0, \quad f_i(\mathbf{p}_i) = 0, \quad \frac{\partial f_i}{\partial n}(\mathbf{p}_i) = 1. \tag{34}$$

This construction ensures that each function ψ_i satisfies Laplace's equation and consequently can also be written in terms of a boundary integral

13

equation

$$c(\mathbf{p}_i)\psi_i(\mathbf{p_i}) + \int_S \psi_i(\mathbf{q})\frac{\partial G}{\partial n}(\mathbf{p}_i, \mathbf{q})dS = \int_S \frac{\partial \psi_i}{\partial n}(\mathbf{q})G(\mathbf{p}_i, \mathbf{q})dS. \qquad (35)$$

Subtracting Eq. (35) from (25) and rearranging the terms so that the unknowns are on the right-hand side gives the modified integral equation

$$\int_S \left[\phi(\mathbf{q}) - \phi(\mathbf{p}_i)\right]\frac{\partial G}{\partial n}(\mathbf{p}_i, \mathbf{q})dS = \int_S \frac{\partial \phi}{\partial n}(\mathbf{q})G(\mathbf{p}_i, \mathbf{q})dS$$
$$+\left(\frac{\partial \phi}{\partial n}\right)_i \int_S \left(f_i(\mathbf{q})\frac{\partial G}{\partial n}(\mathbf{p}_i, \mathbf{q}) - \frac{\partial f_i}{\partial n}(\mathbf{q})G(\mathbf{p}_i, \mathbf{q})\right)dS. \qquad (36)$$

4.1. Choice of functions f_i

The only constraints on the functions f_i are that they satisfy the conditions given in Equation (34). In an infinite domain and in the absence of a wall, we can show that following function satisfies the given constraints [39]

$$f_i(\mathbf{p}) = \frac{|\mathbf{p}_i - \mathbf{p}_D|^2}{\mathbf{n}_i \cdot (\mathbf{p}_i - \mathbf{p}_D)}\left(1 - \frac{|\mathbf{p}_i - \mathbf{p}_D|^2}{|\mathbf{p} - \mathbf{p}_D|^2}\right), \qquad (37)$$

where $\mathbf{p}_D$ is the position vector of an arbitrary point exterior to the bubble with $\mathbf{n}_i \cdot (\mathbf{p}_i - \mathbf{p}_D) \neq 0$. In order to ensure ψ_i are axisymmetric functions, the point $\mathbf{p}_D = (0, 0, z_D)$ is chosen to be located on the z-axis. This ensures that f_i is constant in θ and does not appear in the azimuthal integrals.

For the case of a bubble near a rigid wall f_i must satisfy the additional condition

$$\frac{\partial f_i}{\partial z} = 0 \text{ at } z = 0, \qquad (38)$$

to ensure no integration over the wall is necessary. This, along with the conditions given in Eq. (34), leads to the following form for f_i (details given in Appendix)

$$f_i(\mathbf{p}) = -\left(\frac{\rho_i^3 \bar{\rho}_i^3}{\bar{\rho}_i^3 \sigma_i + \rho_i^3 \bar{\sigma}_i}\right)\left[\left(\frac{1}{\rho} - \frac{1}{\rho_i}\right) + \left(\frac{1}{\bar{\rho}} - \frac{1}{\bar{\rho}_i}\right)\right], \qquad (39)$$

where

$$\rho \equiv \sqrt{r^2 + (z - z_D)^2}, \quad \bar{\rho} \equiv \sqrt{r^2 + (z + z_D)^2},$$
$$\sigma \equiv rn_r + (z - z_D)n_z, \quad \bar{\sigma} \equiv rn_r + (z + z_D)n_z, \qquad (40)$$

and the suffix i indicates evaluation at $\mathbf{p}_i = (r_i, 0, z_i)$.

Note that, in general, a different point $\mathbf{p}_D(i)$ can be chosen for each node if required, to avoid any numerical difficulties.

14

4.1.1. Discretised Equations

The discretised form of Eq. (36) is then

$$\sum_{j=1}^{N} \int_{s_j}^{s_{j+1}} \left(\phi(s) - \phi(\mathbf{p}_i) \right) \beta_i(s) ds + S_\infty^{(1)} = \sum_{j=1}^{N} \int_{s_j}^{s_{j+1}} \frac{\partial \phi}{\partial n}(s) \alpha_i(s) ds$$

$$+ \left(\frac{\partial \phi}{\partial n} \right)_i \left[\sum_{j=1}^{N} \int_{s_j}^{s_{j+1}} f_i(s) \beta_i(s) ds - \sum_{j=1}^{N} \int_{s_j}^{s_{j+1}} \frac{\partial f_i}{\partial n}(s) \alpha_i(s) ds + S_\infty^{(2)} \right], \quad (41)$$

where $S_\infty^{(1)}, S_\infty^{(2)}$ are the non-zero integrals over the 'surface at infinity'

$$S_\infty^{(1)} = -\phi(\mathbf{p}_i) \int_{S_\infty} \frac{\partial G}{\partial n}(\mathbf{p}_i, \mathbf{q}) dS, \quad S_\infty^{(2)} = \left(\frac{\rho_i^2 \bar{\rho}_i^3 + \rho_i^3 \bar{\rho}_i^2}{\bar{\rho}_i^3 \sigma_i + \rho_i^3 \bar{\sigma}_i} \right) \int_{S_\infty} \frac{\partial G}{\partial n}(\mathbf{p}_i, \mathbf{q}) dS$$

$$(42)$$

As $|\mathbf{q}| \to \infty$ we have $G \to 1/r$ and $\partial G/\partial n \to -1/r^2$ and therefore

$$\int_{S_\infty} \frac{\partial G}{\partial n}(\mathbf{p}_i, \mathbf{q}) dS = -4\pi. \quad (43)$$

The functions $\alpha_i(s)$ and $\beta_i(s)$ are the azimuthal integrals

$$\alpha_i(s) = \int_0^{2\pi} G_1(\mathbf{p}_i, s) r(s) d\theta, \quad \beta_i(s) = \int_0^{2\pi} \frac{\partial G_1}{\partial n}(\mathbf{p}_i, s) r(s) d\theta, \quad (44)$$

These integrals can be expressed in terms of the following expressions [40]

$$Ia = \int_0^{2\pi} \frac{d\theta}{(1 - k^2 \cos^2 \frac{\theta}{2})^{3/2}} = \frac{4E(k)}{1 - k}, \quad (45)$$

$$Ib = \int_0^{2\pi} \frac{\cos \theta \, d\theta}{(1 - k^2 \cos^2 \frac{\theta}{2})^{3/2}} = \left(\frac{8}{k} - 4 \right) \frac{E(k)}{1 - k} - \frac{8}{k} K(k), \quad (46)$$

where $K(k)$ and $E(k)$ are the complete elliptic integrals of the first and second kind, respectively. Expressions for $\alpha_i(s)$ and $\beta_i(s)$ can then be found

$$\alpha_i(s) = \frac{4r(s)K(k)}{M}, \quad (47)$$

$$\beta_i(s) = -\frac{4r(s)}{M^3} \left(\left[\frac{dz}{ds}(r + r_i - \frac{2r_i}{k}) - \frac{dr}{ds}(z - z_i) \right] \frac{E(k)}{1 - k} + \frac{2r_i}{k} \frac{dz}{ds} K(k) \right), \quad (48)$$

15

with

$$M = \sqrt{(r(s) + r_i)^2 + (z(s) - z_i)^2}, \quad k(s) = \frac{4r(s)r_i}{M^2}. \tag{49}$$

The complete elliptic integrals can be approximated by

$$K(k) \approx P(x) - Q(x)\ln(x), \tag{50}$$

$$E(k) \approx R(x) - S(x)\ln(x), \tag{51}$$

where $x = 1 - k^2(s)$ and P, Q, R and S are tabulated polynomials [15]. If we assume the velocities vary approximately linearly over each segment Eq. (41) becomes

$$\sum_{j=1}^{N} E_{ij} + 4\pi\phi_i = \sum_{j=1}^{N} \left(B_{ij}\frac{\partial\phi}{\partial n}(s_j) + C_{ij}\frac{\partial\phi}{\partial n}(s_{j+1}) \right)$$

$$+ \left(\frac{\partial\phi}{\partial n}\right)_i \left[\sum_{j=1}^{N}(A_{ij} - D_{ij}) + 4\pi \left(\frac{\rho_i^2\bar{\rho}_i^3 + \rho_i^3\bar{\rho}_i^2}{\bar{\rho}_i^3\sigma_i + \rho_i^3\bar{\sigma}_i} \right) \right] \tag{52}$$

where

$$A_{ij} = \int_{s_j}^{s_{j+1}} f_i(s)\beta_i(s)ds, \tag{53}$$

$$B_{ij} = \int_{s_j}^{s_{j+1}} \left(\frac{s_{j+1} - s}{s_{j+1} - s_j} \right)\alpha_i(s)ds, \tag{54}$$

$$C_{ij} = \int_{s_j}^{s_{j+1}} \left(\frac{s - s_j}{s_{j+1} - s_j} \right)\alpha_i(s)ds, \tag{55}$$

$$D_{ij} = \int_{s_j}^{s_{j+1}} \frac{\partial f_i}{\partial n}(s)\alpha_i(s)ds, \tag{56}$$

$$E_{ij} = \int_{s_j}^{s_{j+1}} \left(\phi(s) - \phi_i \right)\beta_i(s)ds. \tag{57}$$

Eq. (52) for $i = 1, \ldots, N + 1$, is a system of $N + 1$ equations which can be solved for the values of $\partial\phi/\partial n$ at the nodes on the bubble surface. The system can be written in matrix form as

$$\mathbf{Gv} = \mathbf{h}. \tag{58}$$

16

The singularities present in the original BEM are now suppressed. Consequently, a simple Gaussian quadrature can be used over the whole bubble surface. The diagonal entries of G are (for $i \neq 1, N+1$)

$$
\begin{aligned}
G_{ii} &= \sum_{j=1}^{N} \left(A_{ij} - D_{ij} \right) + B_{ii} + C_{i,i-1} - 8\pi \left(\frac{\rho_i^2 \bar{\rho}_i^3 + \rho_i^3 \bar{\rho}_i^2}{\bar{\rho}_i^3 \sigma_i + \rho_i^3 \bar{\sigma}_i} \right) \\
&= \sum_{j=1}^{N} A_{ij} - \sum_{j \neq i, i-1} D_{ij} + \int_{s_i}^{s_{i+1}} \left(\frac{s_{i+1} - s}{s_{i+1} - s_i} - \frac{\partial f_i}{\partial n}(s) \right) \alpha_i(s) ds \\
&\quad + \int_{s_{i-1}}^{s_i} \left(\frac{s - s_{i-1}}{s_i - s_{i-1}} - \frac{\partial f_i}{\partial n}(s) \right) \alpha_i(s) ds - 8\pi \left(\frac{\rho_i^2 \bar{\rho}_i^3 + \rho_i^3 \bar{\rho}_i^2}{\bar{\rho}_i^3 \sigma_i + \rho_i^3 \bar{\sigma}_i} \right). \quad (59)
\end{aligned}
$$

The singularities of $\alpha_i(s_i)$ are suppressed in the above integrals since the terms in brackets tend to zero as $s \to s_i$. The non-singular nature of the integrals was proven in [20] using linear functions for f_i.

4.2. Quintic Splines

The functions ϕ and $\frac{\partial \phi}{\partial n}$ are known at the nodes on the bubble surface. However, in addition to this, the values of these functions at intermediate points are required to approximate the integrals in (53) - (57). Previous studies [22] have used linear elements and assumed ϕ and its normal derivative are linear on each segment. In order to more accurately represent the surface variables we follow the work of Lind and Phillips [26] and use splines. Spline interpolation is desirable since it provides similar results to higher order polynomial interpolation without the problem of Runge's phenomenon.

In order to increase the accuracy of the discretisation and decrease any errors which may arise, quintic splines are considered. The variables are represented in each segment (s_i, s_{i+1}) by a fifth order polynomial

$$
q_i(s) = a_i(s-s_i)^5 + b_i(s-s_i)^4 + c_i(s-s_i)^3 + d_i(s-s_i)^2 + e_i(s-s_i) + f_i, \quad (60)
$$

for some set of constants $(a_i, b_i, c_i, d_i, e_i, f_i)$, for $i = 1, \ldots, N$, the details of which can be found in [42].

The constants $a_i, \ldots, f_i$ in Equation (60) are found by enforcing continuity of the spline and its first four derivatives at each node $\mathbf{p}_i$. Solving these continuity conditions at each node as well as some relevant boundary conditions gives the constants $a_i, \ldots, f_i$ at each segment. The full derivation of these constants can be found in Walters [42].

5. Toroidal Bubble

If a liquid jet forms as the bubble collapses it will eventually impact on the far side of the bubble after which the bubble will enter a toroidal phase. Computationally, this topological singularity needs to be treated carefully. This is achieved by local smoothing of the bubble surface around the impact site. The doubly connected toroidal bubble also imparts a circulation to the flow around the gaseous tube of the toroidal bubble which is accounted for by the introduction of a vortex ring placed inside the bubble.

This vortex ring has strength Γ equal to the circulation in the flow. This is obtained by integrating the tangential velocity around some closed curve C that threads the torus. Taking the bubble surface as this curve gives the circulation as the difference between the potentials ϕ at nodes 1 and $N+1$

$$\Gamma = \oint_C \nabla\phi \cdot d\mathbf{l} = \phi(N+1) - \phi(1), \tag{61}$$

where $d\mathbf{l} = a(-\sin\theta, \cos\theta, 0)d\theta$ is the tangent to the vortex ring. It was shown by Best [3] that for an incompressible potential flow, Γ is constant in time. The exact location of the vortex ring is unimportant provided it lies completely within the bubble. If the vortex ring is too close to a node on the bubble surface, however, numerical instabilities occur. In order to minimise numercial instabilites, the vortex ring is placed as far from the bubble surface as possible.

5.1. Position of the Vortex Ring

To calculate heuristically the internal point furthest from the bubble surface, a grid of Cartesian nodes is calculated in a box containing the bubble. Clearly some of the nodes will not lie inside the bubble and so must be neglected as candidates. If the surface is approximated as straight lines between the bubble nodes, this is a 'point in polygon' problem and thus a ray casting algorithm can be used. Once nodes exterior to the bubble have been discounted the minimum distance to a bubble surface node is calculated for the remaining Cartesian nodes. The height c and radius a of the vortex ring are then defined as the z- and r-coordinates of the furthest point

$$c = z_p, \quad a = r_p. \tag{62}$$

The potential of the bubble is then decomposed into the vortex-ring potential φ^{vr} and a single-valued remnant potential φ

$$\phi(r, z, t) = \varphi^{vr}(r, z) + \varphi(r, z, t). \tag{63}$$

18

The vortex potential, φ^{vr}, is a multivalued function, a single branch of which is selected by introducing an imaginary surface stretching over the ring. The potential φ^{vr} is discontinuous and jumps by an amount Γ over this surface which in this model is taken to coincide with the impact surface (i.e. nodes $1/N+1$), although this is not necessary.

5.2. Calculation of the Vortex Ring Field

In the numerical simulations 'jet impact' is taken to be when node 1, moving with the liquid jet, comes within a distance 0.01 of node $N+1$ (see Fig. 2). This ensures the two sides of the bubble are close enough to approximate jet impact but not too close to cause numerical instabilities.
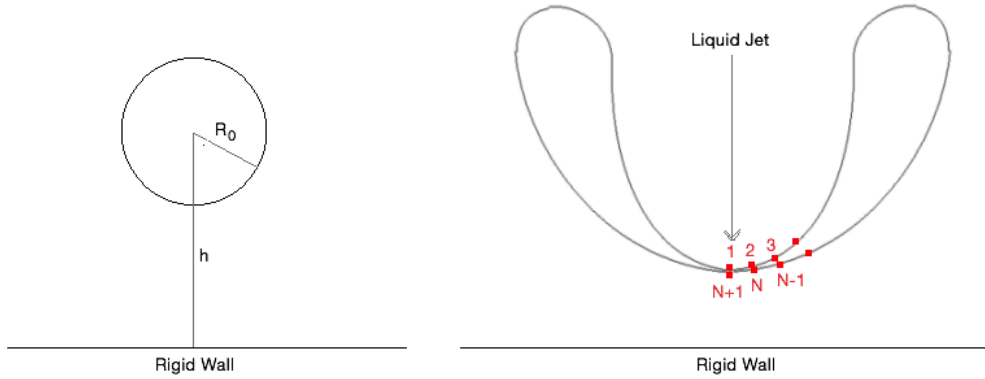
Figure 2: Evolution of bubble prior to jet impact.

In reality, the jet impact represents a physical singularity in time and space which is smeared over time and space by material compressibility and viscosity [47]. For simplicity, however, these effects are not modelled here and the numerical smoothing that takes place due to the discretisation does not represent a physical event. The error introduced as a result of this process is kept sufficiently small through the use of a fine mesh and small time steps. Before the smoothing takes place the remnant potential φ is required; this can be calculated from Eq. (63) following the calculation of the vortex potential φ^{vr}.

The velocity field of a vortex ring of radius a, strength Γ, centered at the

19

origin is [44]

$$\mathbf{v}_0^{vr}(r, z) = \frac{\Gamma}{4\pi} \oint_C \frac{d\mathbf{l} \times (\mathbf{p} - \mathbf{q})}{|\mathbf{p} - \mathbf{q}|^3} = \frac{\Gamma}{4\pi} \oint_C d\mathbf{l} \times \nabla\left(\frac{1}{r}\right), \tag{64}$$

where $\mathbf{p} = (r, 0, z)$, $\mathbf{q} = (a\cos\theta, a\sin\theta, 0)$ and $r = |\mathbf{p} - \mathbf{q}|$. In this application, the vortex ring will never be centred at the origin (since this is located on the rigid wall). To find the velocity field of a ring centred at $z = c$ the method of images is used

$$\mathbf{v}^{vr}(r, z) = \mathbf{v}_0^{vr}(r, z + c) - \mathbf{v}_0^{vr}(r, z - c) = u^{vr}(r, z)\mathbf{i} + w^{vr}(r, z)\mathbf{k}. \tag{65}$$

5.3. Calculation of the Vortex and Remnant Potentials

The vortex potential φ^{vr} at a node can be calculated using solid angles. Using Stokes' Theorem the vortex velocity becomes

$$\mathbf{v}_0^{vr}(r, z) = \frac{\Gamma}{4\pi} \int_S \left(\mathbf{n} \times \nabla\right) \times \left[\nabla\left(\frac{1}{r}\right)\right] dS, \tag{66}$$

where S is any surface with boundary C, from which we derive the following expression for the vortex potential

$$\varphi^{vr}(r, z) = \frac{\Gamma}{4\pi} \int_S \frac{\partial}{\partial n}\left(\frac{1}{r}\right) dS = \frac{\Gamma}{4\pi} \int_S \frac{\cos\alpha}{r^2} dS, \tag{67}$$

where α is the angle between the normal at $\mathbf{q}$ and $\mathbf{r}$. Since $dS\cos\alpha$ is the projection of the area dS on the plane perpendicular to r then $dS\cos\alpha/r^2$ is the elementary solid angle subtended at $\mathbf{p}$ by dS. It then follows that

$$\varphi^{vr}(\mathbf{x}_i) = \frac{\Gamma\Theta(\mathbf{x}_i)}{4\pi}, \tag{68}$$

where $\Theta(\mathbf{x}_i)$ is the solid angle subtended at the point $\mathbf{x}_i$ by the surface of discontinuity which extends over the vortex ring. For simplicity this surface of discontinuity is simply taken as the plane bounded by the ring.

It can be seen that the problem reduces to finding the solid angle of a cone; the formula for which is

$$\Theta(\mathbf{x}_i) = 2\pi\left(1 - \cos\left(\frac{\theta(\mathbf{x}_i)}{2}\right)\right), \tag{69}$$

20
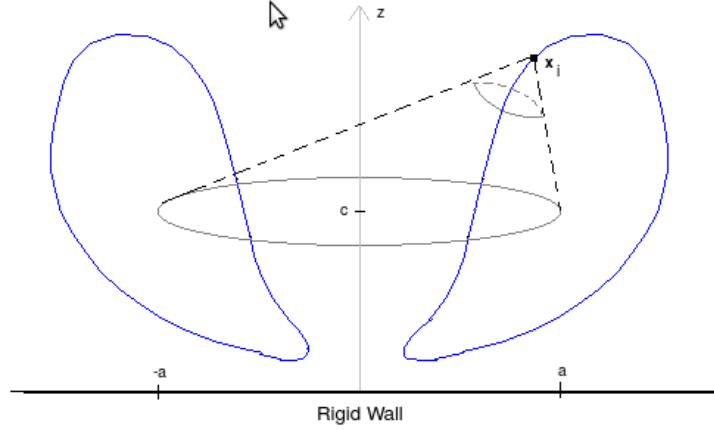
Figure 3: Diagram of the toroidal bubble, vortex ring and the solid angle subtended at a point $\mathbf{x}_i$.

where $\theta(\mathbf{x}_i)$ is the apex angle of the cone. The term $\cos\theta(\mathbf{x}_i)$ can be calculated using the scalar product of the two vectors described by the dashed lines in Fig. 3. The solid angle jumps by 4π over the surface of discontinuity S_c and thus from Equation (68) the vortex potential jumps by an amount equal to Γ. The vortex potential φ^{vr} thus completely accounts for the circulation in the fluid and the remnant potential is smooth everywhere.

The vortex potential has now been found at each node of the bubble surface and the fluid potential is known from the final time step before the transition to toroidal geometry. The remnant potential can then be defined

$$\varphi(r_i, z_i) = \phi(r_i, z_i) - \varphi^{vr}(r_i, z_i), \quad i = 1, \ldots, N+1. \tag{70}$$

This remnant potential is smooth since the discontinuity has been 'removed' by the vortex potential and is now known at the nodes at the instant of jet impact. The bubble is smoothed in order to make the transition from a singly-connected bubble to a doubly-connected toroidal bubble.

5.4. Transition to Toroidal Geometry: Smoothing at Impact Point

Following Wang et. al [44], the impact of the liquid jet is assumed to take place at a single point. Energy is conserved using this model with all the effects of the impact completely transformed into the circulation in the fluid. Since the fluid is incompressible the disturbances are transmitted throughout the fluid at an infinite speed establishing the flow field in the toroidal geometry instantaneously.

21

To model this numerically nodes 1 and $N + 1$ are removed and replaced by a single node located at the mean positions of nodes $1, 2, N$ and $N + 1$ (see Fig. 4). The remnant potential (and all other variables) at this new node is taken as the mean value of its value at these nodes

$$\varphi_{\text{new}}(1) = \varphi_{\text{new}}(N + 1) = \frac{\varphi(1) + \varphi(2) + \varphi(N) + \varphi(N + 1)}{4} \qquad (71)$$
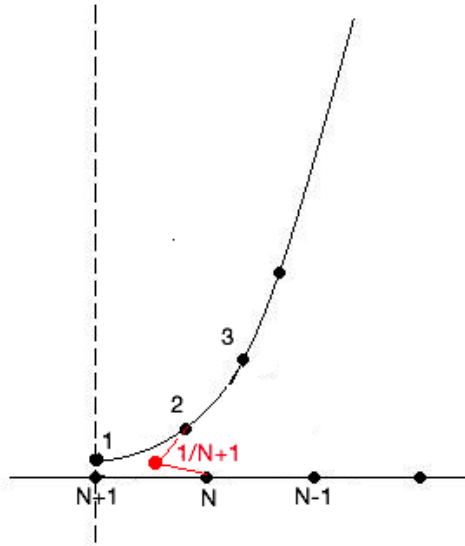
Figure 4: Smoothing of nodes at impact site

Although the distances shown in Fig. 4 are exaggerated, a small amount of bubble volume is lost during smoothing. The number of nodes, N, must be chosen to be large enough so that this loss in volume (and hence in potential energy) is not too large.

5.5. Updating the Remnant Potential

As in the previous section, the surface and surface variables must now be updated to proceed in time. Substituting the decomposed potential (63) into the original bubble evolution equations gives the following dimensionless

system for the evolution of the toroidal bubble

$$\frac{d\mathbf{x}}{dt} = \nabla\varphi + \mathbf{v}^{vr}, \tag{72}$$

$$\frac{d\varphi}{dt} = 1 - \mathbf{v}^{vr} \cdot (\nabla\varphi + \mathbf{v}^{vr}) + \frac{1}{2}|\nabla\varphi + \mathbf{v}^{vr}|^2 - \frac{2E}{Re}\frac{\partial^2\phi}{\partial n^2} - \tau_{nn}^p + \frac{\kappa}{We} - \varepsilon\left(\frac{V_0}{V}\right)^\gamma, \tag{73}$$

$$\frac{d\tau_{nn}^p}{dt} = \frac{1}{De}\left[-\tau_{nn}^p - 2\left(De\tau_{nn}^p - \frac{2(1-E)}{Re}\right)\frac{\partial^2\phi}{\partial n^2}\right]. \tag{74}$$

In order to integrate these equations $\nabla\varphi$, and thus $\partial\varphi/\partial n$, must be found.

5.5.1. Calculation of the Normal Derivative of the Remnant Potential

Since the vortex potential can be written in terms of a potential φ^{vr} it can be seen from Eq. (65) that φ^{vr} satisfies the Laplace equation in the fluid domain and decays at infinity. The remnant potential, therefore, also satisfies the Laplace equation in the fluid domain and decays at infinity and consequently its normal derivative can be found from a modified form of the integral equation (52).

The non-singular formulation described in the previous section is used but for the toroidal bubble the point $\mathbf{p}_D = (0, 0, z_D)$ is always in the fluid domain since it must lie on the vertical axis. This results in the functions f_i (and thus ψ_i) possessing a singularity at the point $\mathbf{p}_D$. This can be removed in a similar manner in which the singularity in G is removed in Eq. (25) resulting in the following integral equation for ψ_i for the case when $\mathbf{p}_D$ in the domain

$$c(\mathbf{p}_i)\psi_i(\mathbf{p}_i) + \int_S \psi_i(\mathbf{q})\frac{\partial G}{\partial n}(\mathbf{p}_i, \mathbf{q})dS = \int_S \frac{\partial \psi_i}{\partial n}(\mathbf{q})G(\mathbf{p}_i, \mathbf{q})dS$$
$$- 4\pi\left(\frac{\rho_i^3\bar{\rho}_i^3}{\bar{\rho}_i^3\sigma_i + \rho_i^3\bar{\sigma}_i}\right)G(\mathbf{p}_i, \mathbf{p}_D)\left(\frac{\partial\psi}{\partial n}\right)_i. \tag{75}$$

Also, nodes 1 and $N+1$ now coincide and setting $\mathbf{p}_1 = \mathbf{p}_{N+1}$, $\phi_1 = \phi_{N+1}$ results in a system of N equations (rather than $N+1$ equations for the singly connected bubble). Since the bubble surface is now closed, periodic boundary conditions are imposed on the quintic splines. The resulting linear system is solved using a Thomas algorithm for periodic systems. Once this system of equations has been solved for $\frac{\partial\varphi}{\partial n}$, the tangential derivative $\frac{\partial\varphi}{\partial s}$ is found using

23

spline interpolation. The remnant potential is now fully determined on the bubble surface and equations (72)-(74) can be solved to evolve the system.

5.6. Calculation of the Normal Derivative of the Potential

The normal derivative of the potential is required when calculating the stress for the toroidal bubble. Although ϕ can be found from (63) at each time step, the normal velocity cannot be found by solving the integral equation since it is multi-valued at the node $1/N + 1$. Instead, use is made of (63) to find the normal velocity in terms of known quantities

$$\frac{\partial \phi}{\partial n} = \frac{\partial \varphi}{\partial n} + u^{vr} n_r + w^{vr} n_z, \tag{76}$$

where $n_r = \frac{\partial r}{\partial n} = \frac{dz}{ds}$, $n_z = \frac{\partial z}{\partial n} = -\frac{dr}{ds}$ are calculated using the spline representation of the bubble surface. Similarly, the tangential velocity is

$$\frac{\partial \phi}{\partial s} = \frac{\partial \varphi}{\partial s} + u^{vr} s_r + w^{vr} s_z, \tag{77}$$

with $s_r = \frac{\partial r}{\partial s}$, $s_z = \frac{\partial z}{\partial s}$.

If the vortex ring is too close to a node it will cause numerical instabilities. To prevent this the radius and height of the ring are recalculated if the minimum distance to the nodes falls below 3 times that of an element length of the bubble surface. When this happens the vortex-ring potential (and remnant potential) must be recalculated and then updated in the manner already described.

As the toroidal bubble re-expands the two sides of the bubble tend to move towards each other as the eye of the torus shrinks. If the bubble comes within 10^{-2} of the vertical axis it is assumed that the bubble 'reconnects' into a singly connected form. In order to carry out this transition the reverse procedure to that implemented at jet impact is performed.

6. Numerical Comparisons

6.1. Validation

To validate the modelling of fluid rheology, the BEM formulation is compared to the direct solution of the Rayleigh-Plesset equation for a spherical bubble in an infinite Oldroyd-B fluid. In Fig. 5, a comparison of the predictions of the evolution of bubble radius is shown for both methods.
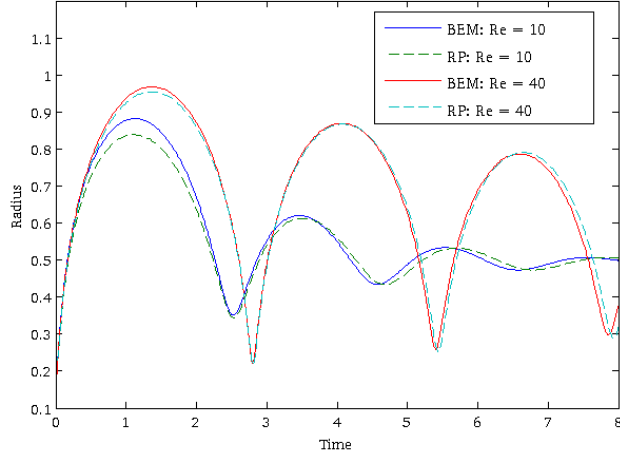
Figure 5: Comparisons of the quintic BEM with the direct solution of the Rayleigh-Plesset equation for an Oldroyd-B fluid with $We = 0$, $De = 0.1$ and $Re = 10$, $Re = 40$.

Excellent agreement is found for both $Re = 10$ and $Re = 40$, indicating that the assumption that the bulk viscosity effects are unimportant is reasonable. Other validations are performed using comparisons with the cubic (singular) formulation of Lind and Phillips [25]. This cubic BEM code is validated in [25] for inviscid and viscous Newtonian fluids.

6.2. Comparison of Non-Singular and Standard BEM Formulations

6.2.1. Instabilities

For an initially spherical bubble in an infinite fluid (neglecting surface tension) the surface should remain spherical and thus any deviation is purely a consequence of numerical error. The following quantity gives an estimate of the numerical error

$$\max\left(r_{dev}(i)\right) = \max\left(|\mathbf{d}_i| - \frac{1}{N+1}\sum_{j=1}^{N+1}|\mathbf{d}_j|\right), \tag{78}$$

where $|\mathbf{d}_i| = \sqrt{r_i^2 + z_i^2}$ and the bubble is centred at the origin. This is the difference between the radius at a node and the mean radius of the bubble. For the standard BEM, a smoothing scheme is typically applied every several time steps to prevent the manifestation of instabilities. In Fig. 6 the deviation from sphericity is plotted against time for both the cubic standard

25

BEM and the quintic non-singular BEM with no smoothing applied. It can be seen that the magnitude of the error is considerably smaller for the non-singular BEM; in fact the standard BEM diverges at $t \approx 4$ (end of second oscillation) as growing instabilities cause unnaturally high velocities. The new non-singular method allows the computations to run until the end of the fourth oscillation before it succumbs to similar problems.
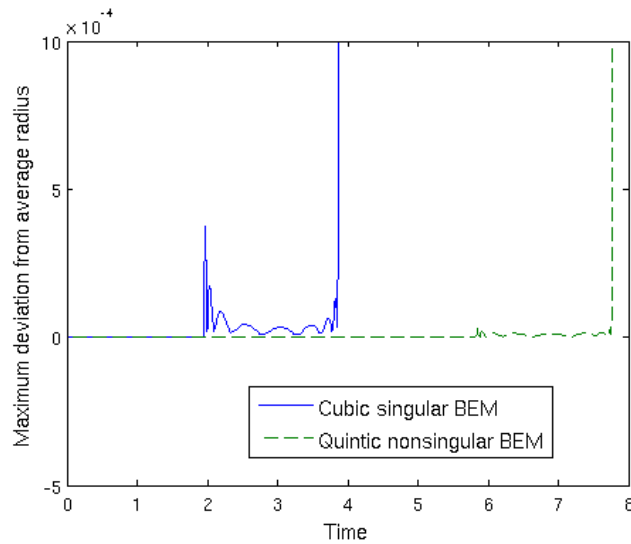
Figure 6: Maximum deviation from average radius with no smoothing and $N = 32$.

For both cases, spikes can be seen at roughly $t = 2, 4, 6, 8$, corresponding to the bubble at minimum volume. At these instances in time the nodes are very close together and errors arise (particularly in the standard BEM) from the influence on the observation node of the singular kernel centred at the nearby node. This can also be seen in Fig. 7 in which bubble surfaces close to jet impact are shown for the case $h = 1.2$, $N = 32$ and no smoothing. Note that the standard BEM failed to converge due to the onset of instabilities causing spurious velocities whereas the non-singular formulation remains smooth and well-behaved until the fourth oscillation. Considering Figs. 6 and 7 it is clear that the non-singular BEM is less susceptible to these instabilities. This agrees with the conclusions of Klaseboer et al. [39] who considered two nearly touching spheres and found numerical errors in the region where the spheres nearly touch using the standard BEM, but not for the non-singular formulation.

26
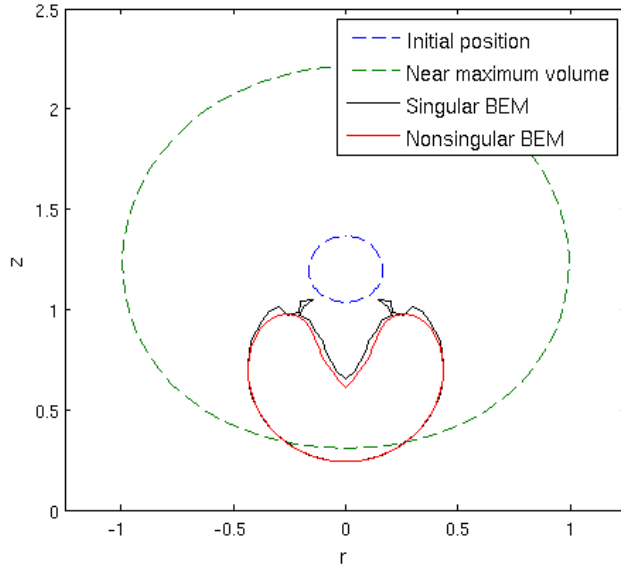
Figure 7: Evolution of the bubble surface as a jet forms for the case $h = 1.2$ and an inviscid fluid with no smoothing applied for the singular BEM (black) and non-singular BEM (red).

7. Model Predictions

7.1. Validation of Geometry Change

In Fig. 8, the normal velocity at the bubble surface is plotted against bubble surface arclength for the singly-connected bubble just before jet impact and for the corresponding toroidal bubble once the impact surface has been smoothed and the vortex ring placed inside the bubble. At the instant of jet impact node 1 is moving rapidly towards the opposite side of the bubble (node $N + 1$) which has a much lower velocity. Once the impact point is smoothed the velocity of the 'new' node $1/N + 1$ takes a value roughly that of the average of the velocities of the previous nodes labelled 1 and $N + 1$. The normal velocities at the remaining nodes (which have not been moved) show good agreement with their values before the transition.

For an inviscid fluid the total energy should remain constant throughout the computations due to the assumption of incompressibility. The impact of the liquid jet is a violent event though and this, along with the change in topology of the fluid domain, results in strong instabilities in the toroidal bubble surface.

27
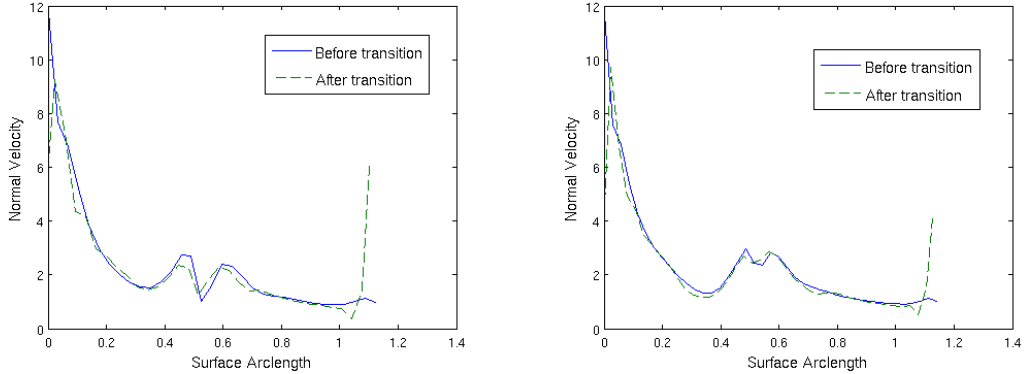
Figure 8: Comparisons of the normal velocities before and after the transition from a singly-connected bubble to a toroidal bubble for $N = 32$ (left) and $N = 40$ (right).

7.2. Inviscid Fluid

To begin, a cavitation bubble in an inviscid fluid is considered. Surface tension is neglected so that the bubble oscillations will be spherical for large stand-off distances. This permits us to measure the numerical error in the BEM code using the departure from sphericity as a test. Although viscous effects will often be important in situations of practical interest, many previous studies [5, 47] have assumed that the fluid is inviscid. This is done for simplicity due to the difficulty of calculating stresses within the fluid since the internal fluid domain is not discretised in the BEM.

In Figs. 9 - 10, the effect of the initial stand-off distance h on the bubble dynamics is shown. This stand-off distance is essentially the distance from the boundary expressed in terms of the initial radius R_0. Fig. 9 shows the relative movement of the bubble centroid C_n from its initial position for $h = 2, 4$ and 8. For the case $h = 8$, there is very little translational movement since the bubble is relatively far from the boundary and is thus not significantly disturbed from spherical oscillations in the first few oscillations shown here. When the initial stand-off distance is reduced to $h = 4$ the proximity of the rigid boundary makes the far side of the bubble accelerate faster than the near side during collapse causing the bubble to migrate towards the boundary. The pressure gradient that is induced normal to the boundary by the asymmetry in the pressure field creates the so-called Bjerknes force [24]. This is particularly prominent at $t \approx 2$ and $t \approx 4$ when the bubble is at the end of the collapse phase.

28
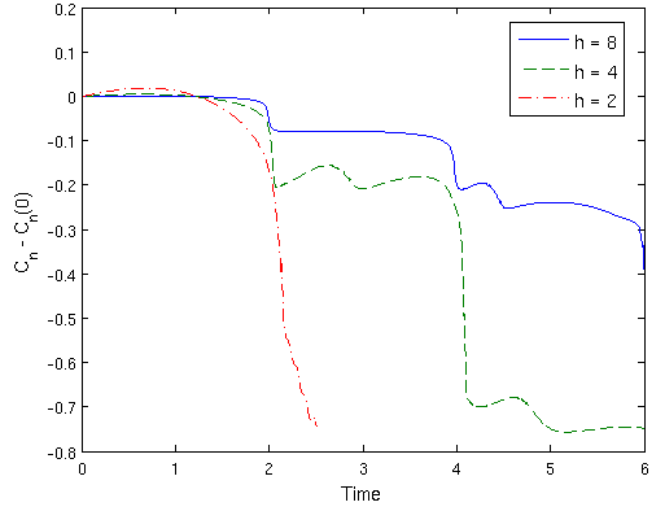
Figure 9: Bubble centroid movement (from initial position) for a bubble in an inviscid fluid with $h = 2, 4$ and 8.
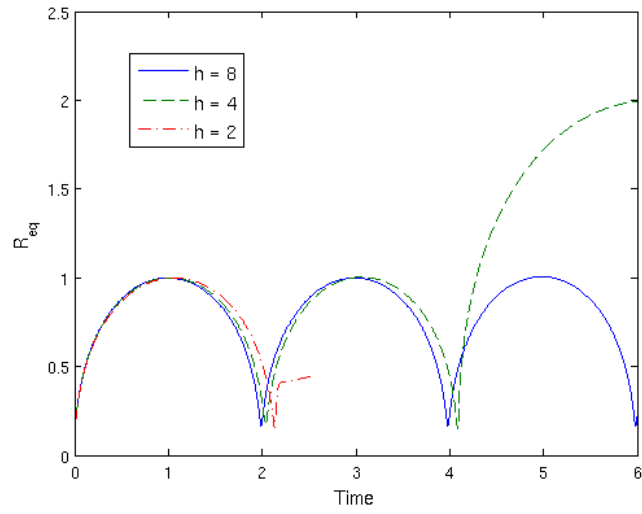
Figure 10: Equivalent bubble radius for a bubble in an inviscid fluid with $h = 2, 4$ and 8.

The equivalent radius, R_{eq}, is defined to be the radius of a spherical bubble having the same volume. This is plotted in Fig. 10. In the primary oscillation cycle there is little difference observed in bubble size except for

29

a slight increase in the oscillation period as h is decreased. For $h = 8$ the stable oscillations between $R_{eq} = R_0$ and $R_{eq} = 1$ continue for the entire simulation, as expected. Similar oscillations occur for the case $h = 4$ until the third growth phase at $t \approx 4$ when the bubble grows to a size of $R_{eq} \approx 2$. This growth occurs during the toroidal phase and may be a result of numerical errors occuring due to the very high jet velocities occuring before impact in this case (see Fig. 14).

When $h = 2$, jet impact occurs near minimum bubble volume at $t \approx 2$. This is a very violent event involving high velocities and a change in topology, resulting in strong instabilities in the toroidal bubble surface. It is not clear to what extent these instabilities are numerical, however, care is taken to minimise spurious velocities by using a small time step and small mesh size on the bubble surface. As the bubble grows the surface becomes smoother which can be seen in Fig. 11 in which snapshots of the bubble surface are plotted.
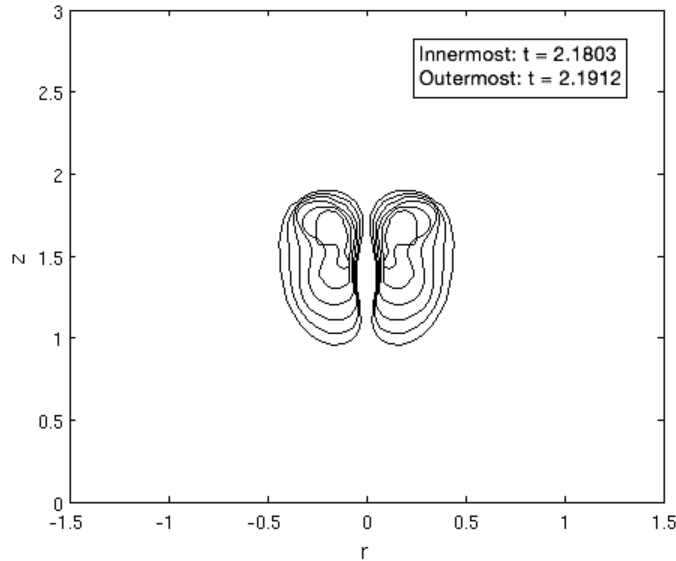
Figure 11: Reexpansion of bubble after transition to a toroidal form for $h = 2$.

Due to the bubble expansion, the aperture of the torus shrinks until the bubble 'reconnects' into a singly-connected form as shown in Fig. 12. Another liquid jet then forms, eventually impacting the rigid wall directly (Fig. 13). At this instant, parts of the bubble surface are very close to the

30

rigid wall resulting in the formation of a very thin fluid film near the wall. This leads to the onset of instabilities and eventually to the termination of the simulation. To combat this, the numerical scheme could be modified to allow the bubble to adhere to the boundary as in Ni et al. [32]. This is left for future work.
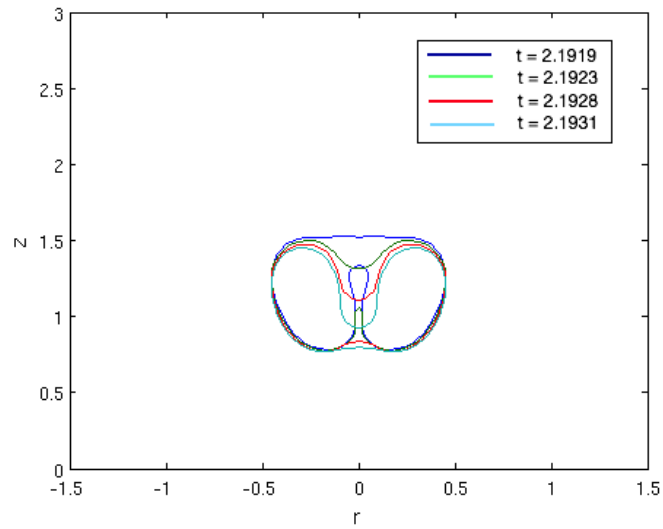
Figure 12: Second singly connected phase after reconnection for $h = 2$.
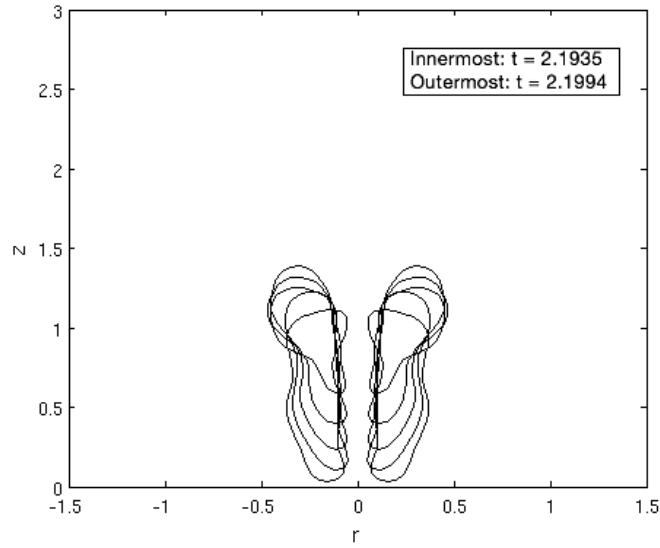
Figure 13: Second toroidal phase for $h = 2$.
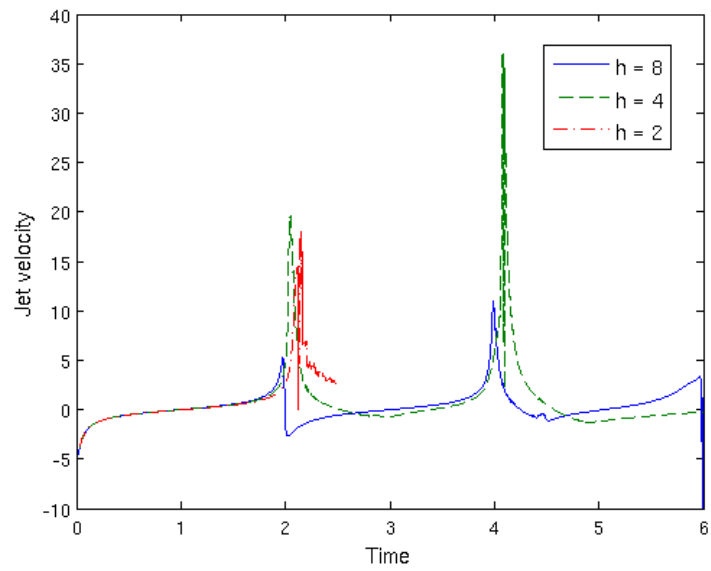
Figure 14: Jet velocities (at node 1) for a bubble in an inviscid fluid with $h = 2, 4$ and 8.

Very high jet velocities are observed near bubble minimum volume for

all the cases considered here (see Fig. 14). The internal gas of the bubble becomes compressed as it shrinks to its minimum volume causing high pressures that are transmitted to the rigid wall. Dimensionless variables are used to produce all the plots (see (22)). Jet velocities as high as 350m/s also occur. High velocity liquid jets have also been shown to potentially damage even strong engineering surfaces.

Qualitatively, these results are in agreement with those obtained in previous studies such as Wang et al. [44]. In Wang et al. [44], however, jet velocities and other quantities are only shown up until jet impact; possibly due to the instabilities present in the toroidal phase which create numerical difficulties when computing jet velocities and pressures.

7.3. Effects of Viscoelasticity

As described in Section 2.2, fluid rheology is introduced approximately through the dynamic boundary condition at the bubble surface given by Eq. 11. In the non-dimensionalised equations, the viscous and viscoelastic properties of the fluid are quantified in terms of the Reynolds (Re) and Deborah (De) numbers.

7.3.1. Effect of Initial Stand-Off Distance

For a bubble in an Oldroyd-B fluid with $Re = 5$ and $De = 1$, the effect of the initial stand-off distance is shown in Figs. 15 - 19. Compared to the inviscid fluid, the bubble centroid does not vary as much (for similar values of h) due to the retarding effect of fluid viscosity on bubble wall velocities. Considering the case $h = 2$, however, a large rebound away from the wall is observed as the bubble expands at $t \approx 2$ and $t \approx 4$. This is due to fluid elasticity and a build up of extra stress as the bubble collapses which is not present in the inviscid case.

Fig. 16 shows the evolution of the equivalent radius for the same parameters as Fig. 15. The maximum radius achieved at each oscillation decreases over time due to viscous dissipation, although little difference is observed for the different values of h considered; other than the slight lengthening of the period of oscillation which was also observed in the inviscid case.
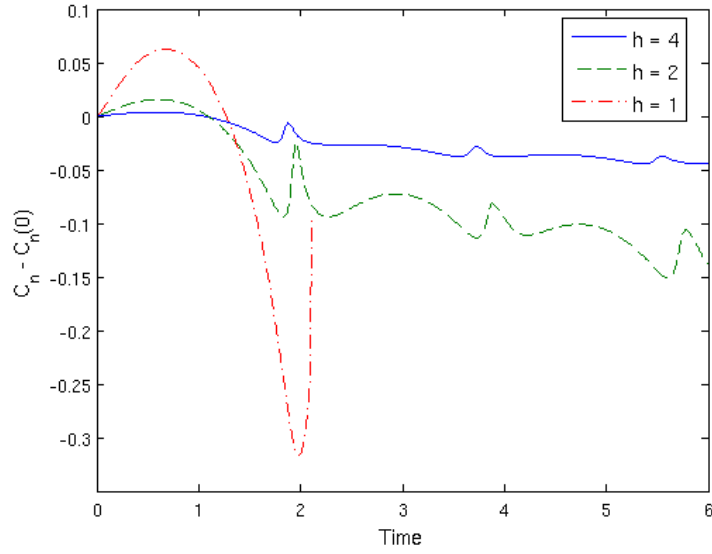
Figure 15: Bubble centroid movement (from initial position) for a bubble in an Oldroyd-B fluid with $Re = 5$, $De = 1$ and $h = 1, 2$ and 4.
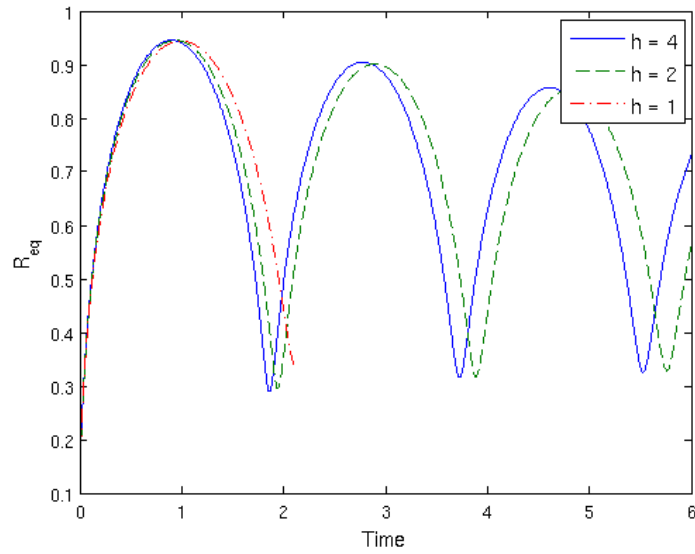
Figure 16: Equivalent radius for a bubble in an Oldroyd-B fluid with $Re = 5$, $De = 1$ and $h = 1, 2$ and 4.

The jet velocities of the bubble wall are shown in Fig. 17. The maximum velocity decreases with decreasing h. The jet velocities are significantly lower than those observed in the inviscid case due to the effects of fluid viscosity. As a result, jet impact (and transition to a toroidal form) does not occur for any of these cases, despite the presence of the rigid boundary.
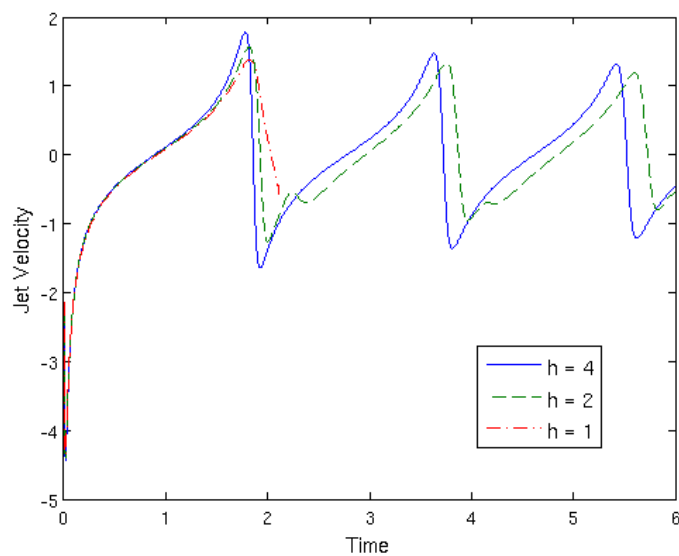
Figure 17: Jet velocity for a bubble in an Oldroyd-B fluid with $Re = 5$, $De = 1$ and $h = 1, 2$ and 4.
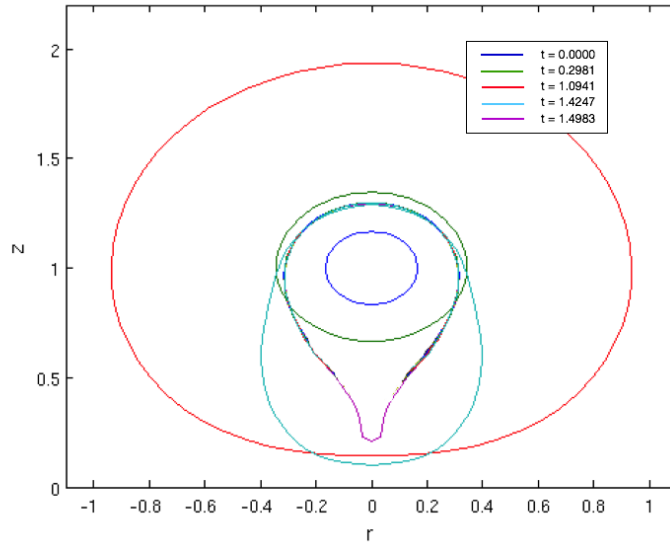
Figure 18: Snapshots of the bubble surface in time for bubble in an Oldroyd-B fluid with $Re = 5$, $De = 1$ and $h = 1$.

7.3.2. Effect of Fluid Viscosity and Fluid Elasticity

The Reynolds number represents the relative importance of inertial and viscous effects. In this section the Reynolds number is varied to investigate its impact on the bubble dynamics. In Figs. 19 - 20 the parameters $h = 2$, $De = 0.5$ are fixed.

The centroid position over time for each case is plotted in Fig. 19. As noted in the previous section, viscosity has a retarding effect on the fluid velocities and thus centroid movement is markedly reduced for low Reynolds numbers. In the case $Re = 1$ the viscous forces completely dominate the inertial forces and almost no translation towards the rigid wall is observed.
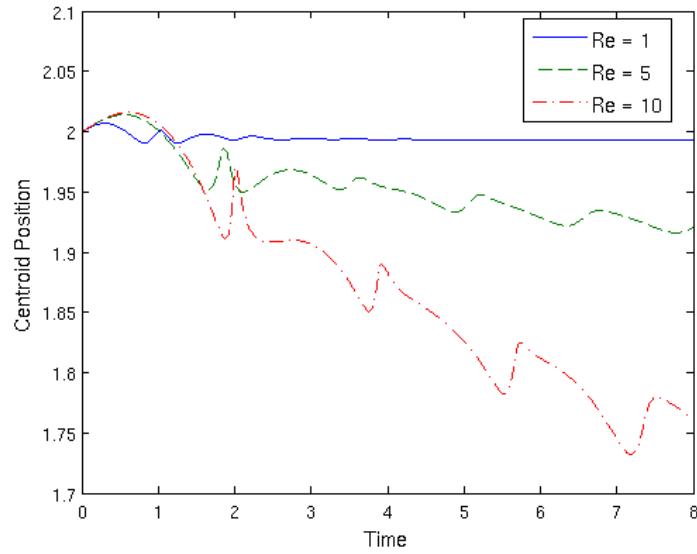
Figure 19: Bubble centroid position for the cases $h = 2$, $De = 0.5$ and $Re = 1, 5$ and 10.

The inhibitive effect of fluid viscosity is also shown in Fig. 20 in which the jet velocities (velocities at node 1) are plotted. In each of the cases shown the bubble undergoes stable oscillations and will reach an equilibrium radius if the simulation is performed for long enough. An increase in Re results in larger velocities.
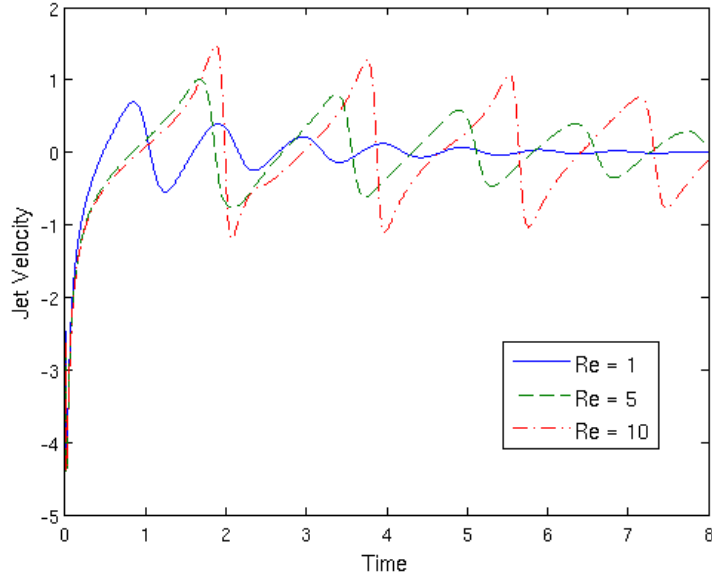
Figure 20: Jet velocities for the cases $h = 2$, $De = 0.5$ and $Re = 1, 5$ and 10.

In the next set of results the value of De is increased to 10. In Figs. 21 - 22 predictions of bubble dynamics are shown for $h = 2$, $Re = 1, 5$ and 10 and $De = 10$. The same trends as the previous results for $De = 0.5$ are observed with a decrease in viscosity (i.e. increasing Re from 1 to 10) resulting in more translational movement, higher velocities and higher pressures produced at the rigid wall. For $De = 10$, however, the elastic effects of the fluid are more dominant and can negate the viscous effects. With $De = 10$ for both cases $Re = 5$ and $Re = 10$ a liquid jet forms, eventually impacting on the far side of the bubble in a similar manner to the inviscid case with $h = 2$. The erratic oscillations in jet velocities present in Fig. 22 occur when the bubble is toroidal in form in a similar manner to the inviscid case although the instabilities are less pronounced due to the stabilising effect of fluid viscosity and the lower velocities.

38
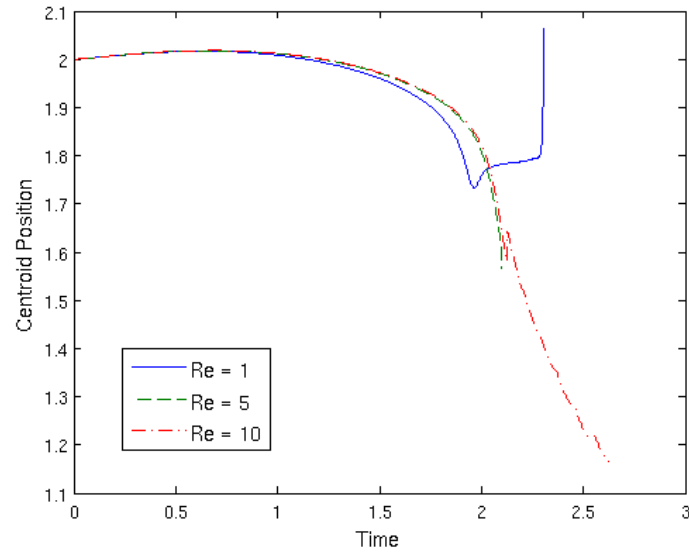
Figure 21: Bubble centroid position for the cases $h = 2$, $De = 10$ and $Re = 1, 5$ and 10.
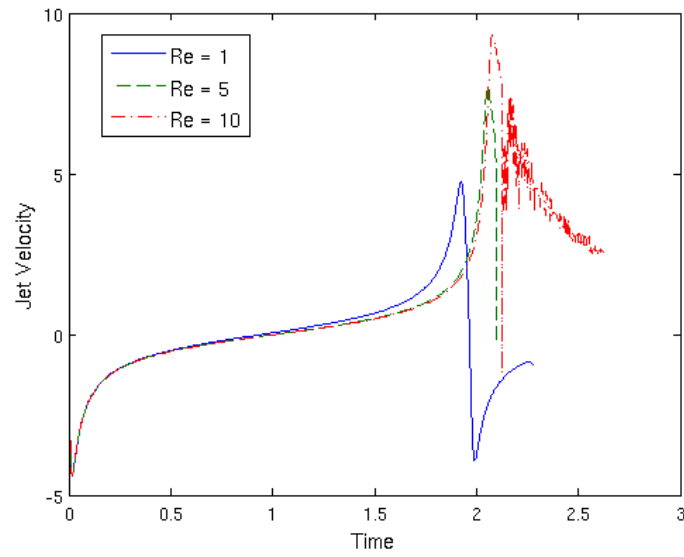
Figure 22: Jet velocities for the cases $h = 2$, $De = 10$ and $Re = 1, 5$ and 10.

Bubble surfaces for the case $Re = De = 10$ and $h = 2$ are shown in Figs.

39

23 - 25. Fig. 23 shows the first singly-connected phase with the formation of the liquid jet. The viscoelasticity of the fluid in this case only has an effect near the end of collapse. The centre of the bubble is thinner than in the inviscid case with two 'lobes' forming either side of a disc-like region. The bubble is still shrinking as jet impact occurs in this case. The rest of the collapse phase is shown in Fig. 24 in toroidal form. Due to the very thin centre of the bubble and fluid elasticity the eye of the torus grows rapidly with the centre of the bubble pulled outwards. The bubble then expands due to its contents, as shown in Fig. 25.
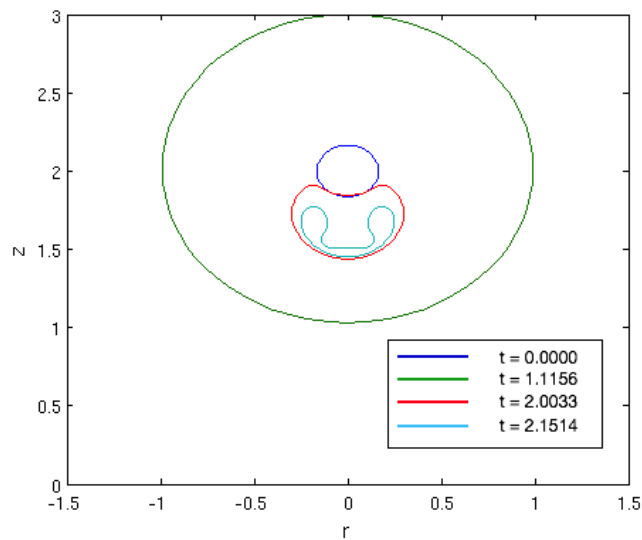
Figure 23: First singly-connected phase for parameters $h = 2$, $Re = De = 10$.
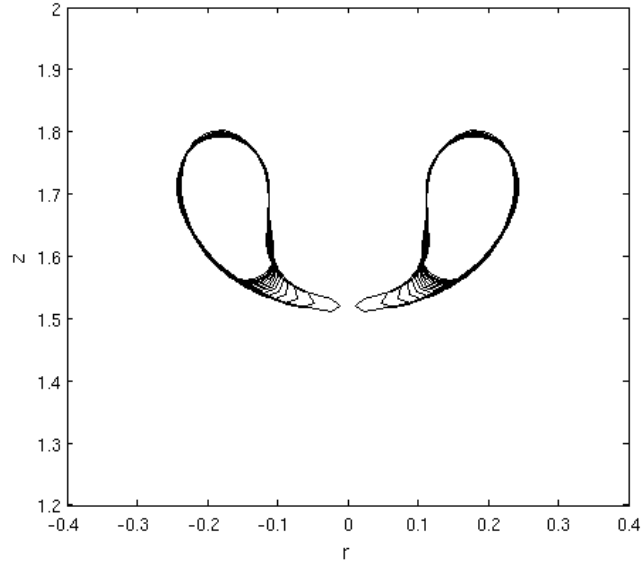
Figure 24: Collapse phase in toroidal form for parameters $h = 2$, $Re = De = 10$. Initial (outer) and final (inner) times are $t \approx 2.101$ and $t \approx 2.148$, respectively.
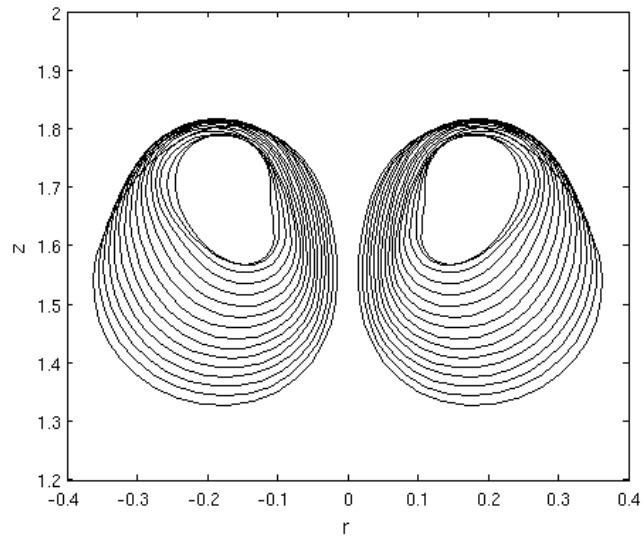
Figure 25: Growth phase in toroidal form for parameters $h = 2$, $Re = De = 10$. Initial (inner) and final (outer) times are $t \approx 2.148$ and $t \approx 2.415$, respectively.

8. Conclusions

A new, non-singular boundary element method for cavitation bubbles has been developed. By reformulating the boundary integral equation, the singularities present due to the Green's function are removed at the outset. By considering a spherical bubble in an infinite fluid, numerical comparisons are made between the standard and non-singular BEM formulations. The instabilities present in the standard BEM are found to be almost completely removed by the new, non-singular formulation since near-singular behaviour no longer occurs when nodes are too close together. A quintic spline discretisation is found to be more accurate than cubic splines, albeit at a slight increase in computational time. For a fixed number of nodes the computational time is approximately doubled for a quintic spline discretisation (108s for $N = 32$ on a standard desktop computer). However, the corresponding error is reduced by at least two orders of magnitude. For more details, the reader is referred to Chapter 3 of the thesis of Walters /citeMWPHD15.

The new non-singular boundary element method is then used to study the dynamics of an initially spherical, gas-filled bubble in an Oldroyd-B fluid near a rigid wall. The diminishing effect of viscoelasticity on jet velocities and pressures has been shown experimentally by Williams et al. [45] as well as numerically, by Lind and Phillips [27], for a material Maxwell model. The dynamics are largely governed by the relative values of the Reynolds and Deborah numbers, though, and jet impact can occur if fluid elasticity is sufficiently high.

If a liquid jet does form for a bubble in an Oldroyd-B fluid the bubble topology at jet impact can be quite distinct from the corresponding Newtonian case. The jet can be considerably broader with the formation of 'lobes' either side of a thin disc-like centre. In the subsequent motion of the bubble following the formation of a toroidal bubble, the bubble rebounds and can move away from the wall. As a result, negative pressures occur at the rigid wall which is a feature not observed for a bubble in an inviscid fluid. A decrease in viscosity also leads to higher velocities and pressures produced, demonstrating a potential reduction of damage to nearby surfaces due to the bubble oscillations.

Acknowledgements

his BEM code which provided the basis for comparisons between the non-singular and standard BEM formulations. The authors would also like to thank the reviewers for their constructive comments which have improved the manuscript.

AppendixA. Choice of function for non-singular BEM

The functions f_i $(i = 1, \ldots, N + 1)$ in (33) must satisfy the following conditions

$$\nabla^2 f_i(r, z) = 0, \text{ in } \Omega, \tag{A.1}$$

$$f_i(r_i, z_i) = 0, \tag{A.2}$$

$$\frac{\partial f_i}{\partial n}(r_i, z_i) = 1, \tag{A.3}$$

$$\frac{\partial f_i}{\partial z}(r, 0) = 0. \tag{A.4}$$

A particular solution to Laplace's equation (A.1) is

$$f_i(r, z) = A + \frac{B}{|\mathbf{x} - \mathbf{x}_D|} + \frac{C}{|\mathbf{x} - \mathbf{x}_D'|}, \tag{A.5}$$

where A, B, C are constants and $\mathbf{x} = (r\cos\theta, r\sin\theta, z)$. The points $\mathbf{x}_D = (0, 0, z_D)$ and $\mathbf{x}_D' = (0, 0, z_D')$ do not lie in the bubble. Eqn. (A.2) implies

$$A = -\frac{B}{|\mathbf{x}_i - \mathbf{x}_D|} - \frac{C}{|\mathbf{x}_i - \mathbf{x}_D'|}. \tag{A.6}$$

Differentiating f_i then gives

$$\frac{\partial f_i}{\partial n} = -B\frac{\sigma}{\rho^3} - C\frac{\sigma'}{\rho'^3} \tag{A.7}$$

with

$$\rho \equiv \sqrt{r^2 + (z - z_d)^2}, \quad \rho' \equiv \sqrt{r^2 + (z + z_d)^2}, \tag{A.8}$$

$$\sigma \equiv rn_r + (z - z_d)n_z, \quad \sigma' \equiv rn_r + (z + z_d)n_z, \tag{A.9}$$

Condition (A.3) gives

$$-B\frac{\sigma_i}{\rho_i^3} - C\frac{\sigma_i'}{\rho_i'^3} = 1. \tag{A.10}$$

The final condition (A.4) leads to following relation

$$\frac{Bz_D}{(r^2 + z_D^2)^{3/2}} + \frac{Cz_D'}{(r^2 + z_D'^2)^{3/2}} = 0, \tag{A.11}$$

which has a solution

$$z_D' = -z_D, \quad B = C. \tag{A.12}$$

Finally, solving Eqns (A.6),(A.10) and (A.12) for A, B and C and substituting them into (A.5) yields the expression for f_i

$$f_i(\mathbf{p}) = -\frac{\rho_i^3 \bar{\rho}_i^3}{\bar{\rho}_i^3 \sigma_i + \rho_i^3 \bar{\sigma}_i} \left[\left(\frac{1}{\rho} - \frac{1}{\rho_i} \right) + \left(\frac{1}{\bar{\rho}} - \frac{1}{\bar{\rho}_i} \right) \right]. \tag{A.13}$$

References

[1] G. K. Batchelor. *An Introduction to Fluid Dynamics.* Cambridge University Press, London, 1967.

[2] T. B. Benjamin and A. T. Ellis. The collapse of cavitation bubbles and the pressures thereby produced against solid boundaries. *Phil. Trans. R. Soc. Lond*, 1966.

[3] J. P. Best. The formation of toroidal bubbles upon the collapse of transient cavities. *J. Fluid Mec. A.*, 251:79–107, 1993.

[4] J. R. Blake. The Kelvin impulse: Application to cavitation bubble dynamics. *J. Austral. Math. Soc.*, 30:127–146, 1988.

[5] J. R. Blake, B. B. Taib, and G. Doherty. Transient cavities near boundaries. Part 1. Rigid boundary. *J. Fluid Mech.*, 170:479–497, 1986.

[6] J. R. Blake, B. B. Taib, and G. Doherty. Transient cavities near boundaries. Part 2. Free surface. *J. Fluid Mech.*, 181:197–212, 1987.

[7] C. E. Brennen. *Cavitation and Bubble Dynamics.* Oxford University Press, Oxford, 1995.

[8] E. A. Brujan. The equation of bubble dynamics in a compressible linear viscoelastic liquid. *J. Fluid Dyn. Res.*, 29:287–294, 2001.

[9] E. A. Brujan. Cardiovascular cavitation. *Med. Eng. Phys.*, 31:742–751, 2009.

[10] E. A. Brujan, T. Ikeda, and Y. Matsumoto. Dynamics of ultrasound-induced cavitation bubbles in non-Newtonian liquids and near a rigid boundary. *Phys. Fluids*, 16:2402, 2004.

[11] E. A. Brujan, G. S. Keen, A. Vogel, and J. R. Blake. the final stage of the collapse of a cavitation bubble close to a rigid boundary. *Phys. Fluids*, 14:85–92, 2002.

[12] G. Chahine and A. Bovis. Pressure field generated by nonspherical bubble collapse. *J. Fluids Eng.*, 105:356–362, 1983.

[13] G. Chahine and A. Bovis. Pressure field generated by nonspherical bubble collapse. *J. Fluids Eng.*, 105:356–362, 1983.

[14] L. Guerri, G. Lucca, and A. Prosperetti. A numerical method for the dynamics of non-spherical cavitation bubbles. In *Proc. 2nd Int. Colloq. on drops and bubbles*, page 175, 1981.

[15] C. Hastings. *Approximations for Digital Computers*. Princeton University Press, Princeton, N.J., 1995.

[16] E. Johnsen and T. Colonius. Numerical simulations of non-spherical bubble collapse. *J. Fluid Mech.*, 629:231âĂŞ–262, 2009.

[17] D. D. Joseph, T. Funada, and J. Wang. *Potential Flows of Viscous and Viscoelastic Liquids*. Cambridge University Press, Cambridge, 2007.

[18] D. D. Joseph and T. Y. Liao. Potential flows of viscous and viscoelastic fluids. *J. Non-Newtonian Fluid Mech.*, 265:1–23, 1994.

[19] E. Klaseboer and B. C. Khoo. An oscillating bubble near an elastic material. *J. Appl. Phys.*, 96:5808–5818, 2004.

[20] E. Klaseboer, Q. Sun, and D. Chan. Non-singular boundary integral methods for fluid mechanics applications. *J. Fluid Mech.*, 696:468–478, 2012.

[21] E. Klaseboer, C. Turangan, S. W. Fong, T. G. Liu, K. C. Hung, and B. C. Khoo. Dimulations of pressure pulse-bubble interaction using boundary element method. *Comput. Meth. Appl. Mech. Engrg.*, 195:4287–4302, 2006.

[22] W. Lauterborn. Cavitation bubble dynamics - new tools for an intricate problem. *Appl. Sci. Res.*, 38:165–178, 1982.

[23] W. Lauterborn and H. Bolle. Experimental investigations of cavitation-bubble collapse in the neighbourhood of a solid boundary. *J. Fluid Mech.*, 72:391–399, 1975.

[24] S. C. Li, editor. *Cavitation of Hydraulic Machinery*, London, 2000. Imperial College Press.

[25] S. J. Lind. *A Numerical Study of the Effect of Viscoelasticity on Cavitation and Bubble Dynamics.* PhD thesis, Cardiff University, 2010.

[26] S. J. Lind and T. N. Phillips. Spherical bubble collapse in viscoelastic fluids. *J. Non-Newtonian Fluid Mech*, 165, 2010.

[27] S. J. Lind and T. N. Phillips. The influence of viscoelasticity on the collapse of cavitation bubbles near a rigid boundary. *Theor. Comp. Fluid Dyn.*, 26(1-4):245–277, 2012.

[28] S. J. Lind and T. N. Phillips. The effect of viscoelasticity on the dynamics of gas bubbles near free surfaces. *Phys. Fluids*, 25:022104, 2013.

[29] D. L. Miller, S. V. Pislaru, and J. F. Greenleaf. Sonoporation: Mechanical DNA delivery by ultrasonic cavitation. *Somat cell molec gen*, 27:115–134, 2002.

[30] T. M. Mitchell, C. L. Kling, R. Cheesewright, and F. G. Hammitt. Numerical and photographic studies of axisymmetric bubble collapse, 1983.

[31] C. Naude. *On the mechanism of cavitation damage by non-hemispherical cavitites collapsing in contact with a solid boundary.* PhD thesis, California Institute of Technology, 1960.

[32] B. Y. Ni, A. M. Zhang, and G. X. Wu. Numerical and experimental study of bubble impact on a solid wall. *J. Fluid Eng*, 137(3):1–16, 2015.

[33] R. G. Owens and T. N. Phillips. *Computational Rheology.* Imperial College Press, London, 2000.

[34] M. Plesset and R. Chapman. Collapse of an initially spherical vapour cavity in the neighbourhood of a solid boundary. *J. Fluid Mech.*, 47:283–290, 1971.

[35] J. J. Rassweiler, T. Knoll, K. Köhrmann, J. A. McAteer, J.E. Lingeman, R. O. Cleveland, M. R. Bailey, and C. Chaussy. Shock wave technology and application: An update. *Eur. Urol.*, 59(5):784–796, 2011.

[36] M. Rattray. *Perturbation effects in cavitation bubble dynamics.* PhD thesis, California Institute of Technology, 1951.

[37] Lord Rayleigh. On the pressure developed in a liquid during the collapse of a spherical cavity. *Phil. Mag.*, 34:94–98, 1917.

[38] K. K. So, X. Y. Hu, and N. A. Adams. Anti-diffusion interface sharpening technique for two-phase compressible ïňĆow simulations. *J. Comput. Phys.*, 231:4304âĂŞ–4323, 2012.

[39] Q. Sun, E. Klaseboer, B. C. Khoo, and D. Y. C. Chan. A robust and non-singular formulation of the boundary integral method for the potential problem. *Eng. Anal. Bound. Elem.*, 43:117–123, 2014.

[40] B. B. Taib. *Boundary integral method applied to cavitation bubble dynamics.* PhD thesis, University of Wollongong, 1985.

[41] Y Tomita, PB Robinson, RP Tong, and JR Blake. Growth and collapse of cavitation bubbles near a curved rigid boundary. *Journal of Fluid Mechanics*, 466:259–283, 2002.

[42] M. J. Walters. *An Investigation into the Effects of Viscoelasticity on Cavitation Bubble Dynamics with Applications to Biomedicine.* PhD thesis, Cardiff University, 2015.

[43] Q. X. Wang, K. S. Yeo, B. C. Khoo, and K. Y. Lam. Strong interaction between a buoyancy bubble and a free surface. *Theor. Comput. Fluid Dyn.*, 8:73–88, 1996.

[44] Q. X. Wang, K. S. Yeo, B. C. Khoo, and K. Y. Lam. Vortex ring modelling of toroidal bubbles. *Theor. Comput. Fluid Dyn.*, 19:303–317, 2005.

[45] P. R. Williams, P. M. Williams, and S. W. J. Brown. A study of liquid jets formed by bubble collapse under shock waves in elastic and newtonian liquids. *J. Non-Newtonian Fluid Mech.*, 76:307–325, 1998.

[46] H. C Yeh and W. J. Yang. The dynamics of gas bubbles moving in liquids with pressure gradients. *J. Appl. Phys.*, 39:3156–3165, 1968.

[47] Y. L. Zhang, K. S. Yeo, B. C. Wang, and C. Wang. 3D jet impact and toroidal bubbles. *J Comput. Phys.*, 166:336–360, 2001.